International Journal of Hydrogen Energy 202 (2026) 153042

Contents lists available at ScienceDirect

International Journal of Hydrogen Energy

journal homepage: www.elsevier.com/locate/he

Design, optimization, and integration of passively-insulated liquid hydrogen tanks for sustainable aviation

Sergio Bagarello [a,b], Ali Elham [c], Ivano Benedetti [a,b,*]

[a] Department of Engineering, University of Palermo, Viale delle Scienze, Edificio 8, 90128, Palermo, Italy
[b] Sustainable Mobility Center, Centro Nazionale per la Mobilità Sostenibile - MOST, Italy
[c] Department of Aeronautics and Astronautics, University of Southampton, University Road, SO17 1BJ, Southampton, United Kingdom

ARTICLE INFO

Keywords:
Hydrogen tank optimization
Composite pressure vessel
Cryogenic storage
Finite element simulation
Sustainable aviation

ABSTRACT

A framework for the optimization of hydrogen pressure vessels is developed based on a passively insulated sandwich-composite architecture, aiming to combine high gravimetric efficiency and low boil-off rate for aircraft applications. The proposed computational tool integrates multiphysics finite-element modelling with nonlinear constraint-based multidisciplinary optimization, accounting for realistic features such as standardized safety factors, airframe integration, non-spherical domes, refuelling cutouts, and anti-sloshing baffles. The optimal design space of such storage systems is explored, showing that all-metal constructions strongly penalize performance, yielding gravimetric efficiencies below 30%. Conversely, composite-based tanks achieve up to 50% efficiency with mass reductions of 57% even when realistic features are included. Scaling effects are assessed, integrating the optimized system into a sustainable aircraft concept and identifying directions to mitigate the performance gap with conventional kerosene-fuelled aviation.

1. Introduction

Anthropogenic activities are a major driver of global warming, leading to significant environmental consequences. Aviation currently accounts for a relatively small amount of global annual carbon emissions, about 2.5%. However, in absence of disruptive measures, this share is projected to rise to 25% by the year 2050 pushing stakeholders, academia and regulatory agencies, to investigate solutions to improve this sector sustainability [1].

Short-term emission reductions can be achieved through improved air traffic management and optimized flight trajectories [2], while advanced lightweight materials such as thermoplastic composites [3] can enhance fuel efficiency and recyclability. Novel aircraft configurations – such as blended-wing-body [4] or Flying-V [5] concepts – offer aerodynamic advantages but demand major regulatory and industrial shifts. Alternative energy carriers also attract attention. Electrochemical batteries, though clean and quiet, remain unsuitable for medium- and long-range missions due to low energy density. Ammonia (NH_3) provides carbon-free combustion but introduces severe toxicity and handling issues [6]. Sustainable aviation fuels (SAFs) derived from biomass or waste are compatible with existing systems yet limited by availability and uncertain long-term sustainability [7].

In this context, *hydrogen* (H_2) is driving interest as an energy carrier due to its virtually unlimited availability, its appealing *gravimetric energy density*, and clean combustion characteristics, resulting in zero carbon dioxide (CO_2) direct emissions [8]. Recent advances in hydrogen production, such as highly active transition-metal electrocatalysts for water splitting [9], further strengthen the prospects of a future hydrogen economy, although the present work focuses exclusively on onboard storage and aircraft integration. This fuel has already been used in several airborne applications [10] that highlighted significant technical challenges stemming from its peculiar properties. While issues linked to green hydrogen production, infrastructure scaling [11], engine modifications [12], and, possibly, contrails formation [13], indeed persist, poor performance of on-board H_2 storage is considered one of the main barriers to widespread adoption in mass- and volume-sensitive applications as aviation [14].

The main constraint arises from hydrogen's low *volumetric energy density* which, being around three times lower than that of conventional Jet A-1, requires specialized storage solutions to achieve sufficient energy capacity within practical volumes. Hence, depending on the application, storage relies on highly compressed gas (GH_2), which, despite its limited gravimetric efficiency ($\approx 2-6\%$), is considered more suitable for short-range applications [15], owing to its relative system simplicity, or, cryogenic liquid hydrogen (LH_2). The latter offers significantly higher storage system energy density and is therefore more appropriate

* Corresponding author at: Department of Engineering, University of Palermo, Viale delle Scienze, Edificio 8, 90128, Palermo, Italy.
E-mail address: ivano.benedetti@unipa.it (I. Benedetti).

https://doi.org/10.1016/j.ijhydene.2025.153042
Received 10 October 2025; Received in revised form 10 December 2025; Accepted 13 December 2025
Available online 16 December 2025

Nomenclature

α	Coefficient of thermal expansion [1/K]
a	Semimajor axis of the hemi-ellipsoidal tank dome [m]
b	Semiminor axis of the hemi-ellipsoidal tank dome [m]
C_p	Specific heat capacity [J/kgK]
D_{co}	Diameter of the circular refuelling cutout [m]
D_{BHc}	Diameter of the bulkhead central opening [m]
D_{BHr}	Diameter of the bulkhead four radial holes [m]
D_f	Internal fuselage diameter [m]
D_{text}	External tank diameter [m]
D_{tint}	Internal tank diameter [m]
E	Young's modulus [GPa]
ϵ	Optimality tolerance
$\nabla F(t)$	Gradient function slope
G	Shear modulus [GPa]
η_{tank}	Gravimetric efficiency of tank [%]
$\nabla H(t)$	Hessian matrix
h_c^{ext}	External convective heat transfer coefficient [W/m^{2}K]
λ_v	Latent heat of vaporization [kJ/kg]
L	Length of the cylindrical tank region [m]
μ	Barrier parameter
k	Thermal conductivity [W/mK]
ν	Poisson's ratio
$\bar{\sigma}_y^{\text{mat}}$	Material yield strength [MPa]
ρ	Density [kg/m^3]
ρ_{ag}	Kreisselmeier–Steinhauser aggregation parameter
Q	Total heat flux environment to inner cavity [W]
ϕ	Tank aspect ratio
R	Radius of tank [m]
S	Internal surface area [m^2]
σ_{11}, σ_{22}, σ_{12}	Local material frame stresses [MPa]
σ_{eq}	von Mises equivalent stress [MPa]
S_{l}	Longitudinal shear strength [MPa]
S_{t}	Transverse shear strength [MPa]
s_k	Step vector
t_{Al}	Thickness of the aluminium layer [mm]
t_{CFRP}	Thickness of the composite layer [mm]
t_j	Vector of the design variables
t_{PUR}	Thickness of the polyurethane layer [mm]
t_{Ti}	Thickness of the titanium alloy layer [mm]
Δt	Step size
T_{ext}	Temperature of the external tank surface [K]
T_{fus}	Temperature of the fuselage environment [K]
T_{ref}	Reference temperature [K]
V	Volume [m^3]
W_{cw}	Catwalk width [m]
X_{c}	Longitudinal compressive strength [MPa]
X_{t}	Longitudinal tensile strength [MPa]
Y_{c}	Transverse compressive strength [MPa]
y_k	Gradient-difference vector
Y_{t}	Transverse tensile strength [MPa]

for medium- and long-range missions, although it generally requires additional subsystems to handle cryogenic conditions [16]. Regardless, hydrogen pressure vessels are typically bulky and heavy, introducing significant penalty compared to conventional kerosene-powered aircraft, where fuel is efficiently stored within the wing structure at ambient temperature and pressure. This study therefore investigates liquid hydrogen vessels, as the use of cryogenic temperatures allows for significantly lower storage pressures (< 2 bar *vs.* up to 800 bar for GH_2), decreasing the structural weight of the tank, thereby enhancing storage efficiency and aircraft range. Studies suggest that only through the adoption of LH_2 can the energetic and economic viability of hydrogen-powered aviation be realized: notably, a critical gravimetric efficiency threshold defines the point beyond which H_2-fuelled aircraft outperform conventionally powered counterparts of comparable size [8,17].

However, for hydrogen to maintain its liquid phase demanding conditions are required. To achieve and sustain temperatures of ≈ 20 K diverse thermal insulation methods can be utilized. Among available insulation techniques, *active* solutions – such as vacuum systems or active cooling – offer excellent thermal performance but at the cost of added mass, complexity, and reliability concerns [18]. *Multilayer insulation*, though lighter, suffers from dimensional instability under repeated cryogenic cycles [19]. Conversely, *foam-based spray-on insulation* provides a simple, robust, and lightweight passive alternative, motivating the present adoption of a composite sandwich pressure vessel optimized for improved gravimetric efficiency [20].

Several studies have been recently published with the intent of advancing the technology readiness level (TRL) of liquid hydrogen storage for aviation. Notably, Adler et al. [21] modelled and optimized the convoluted physics governing LH_2 tanks, with a particular focus on assessing the thermal performance and fuel-ambient interaction in vacuum-insulated architectures. Both Gomez et al. [22] and Tzoumakis et al. [23] conducted finite-element (FE) simulations of all-metal, foam-insulated tanks, demonstrating the feasibility of this architecture, but without optimizing the layout from a thermo-mechanical perspective nor providing pragmatic insight on the design space of such components. Hence, while these contributions indeed offer useful comprehension of the principles of LH_2 storage vessels, a gap remains in literature concerning computational model-based optimization approaches that integrate both practical design strategies – such as composite materials, realistic features, and aircraft integration – and numerical methods to systematically enhance tank performance and narrow the gap with conventional storage systems.

The main contribution of this study is the development of a novel framework for the design and optimization of high-performance cryogenic hydrogen tanks for aviation. The proposed tool integrates finite-element thermo–mechanical analysis with nonlinear constrained optimization to determine the benchmark performance of LH_2 tanks. This integration, although based on established individual methods represents a novel approach in the context of aeronautics, where cryogenic storage introduces additional specific challenges such as strict mass and volume constraints. Within this framework, the optimized design space of *passively-insulated sandwich-composite* vessels is explored, enabling the identification of configurations that minimize system weight while meeting regulations and performance standards. Furthermore, the proposed methodological framework also considers the effects of often neglected pragmatic integration features such as regulations derived safety margins, refuelling cutouts, anti-sloshing baffles, and realistic airframe mounting approaches, which considerably affect the storage system efficiency. The framework is employed to evaluate and compare the impact of practical design parameters, including material selection, tank geometry, and the incorporation of openings for fuel line interfaces as well as anti-sloshing devices to mitigate fluid motion under acceleration. Finally, a vessel design featuring practical additions and tailored to an advanced sustainable airframe concept is presented and areas of possible improvement identified.

This manuscript is structured as follows: Section 2 introduces the passively-insulated composite architecture, detailing the methodology

adopted for its finite-element modelling and integration within the optimization framework. In Section 3 each tank configuration is introduced, justified, and optimized. Comparative results are discussed with particular attention to system-level integration within a specific aircraft concept. Section 4 gathers findings, formulating a critical analysis of performance drivers and outlining directions for future development. Finally, Section 5 summarizes the main contributions and concluding remarks.

2. The composite sandwich tank: definition, modelling, and optimization

This section outlines the proposed methodological framework, introducing the tank conceptual design and its layered architecture, the performance metrics adopted, and the numerical model used to simulate the thermo-mechanical behaviour of the LH_2 vessel. Finally, the optimization problem – formulated with safety-factor-based constraints – is defined and integrated into the framework to iteratively refine the design towards the optimal configuration.

2.1. LH_2 tank design

Given the currently low maturity and standardization of liquid hydrogen tank integration strategies in aviation, the vessel examined in this study is conceived to maximize modularity and scalability across different airframe architectures. The vessel is therefore designed as a *non-integral* unit, that is, a self-supporting structure independent from the aircraft fuselage and not involved in primary load transfer. Unlike integral tanks that are embedded within the aircraft airframe, the non-integral configuration is selected since it allows greater freedom in defining shape, dimensions, and layout.

2.1.1. Geometric considerations

The geometry of cryogenic pressure vessels plays an active role in thermal management and stress distribution. From a thermal standpoint, shapes with minimal surface-to-volume ratio exhibit superior performance [24]. For instance, a spherical tank minimizes discontinuities and, since thermal inflow is roughly proportional to the tank surface area, that has a direct effect on H_2 vaporization rate. Concurrently, large spherical vessels would pose significant challenges in terms of *spatial integration* [25] i.e. the arrangement of passengers, payload, structural elements, fuel, and equipment into a feasible aircraft layout. A pragmatic approach is therefore required, favouring tank shapes that efficiently utilize the available volume, such as cylinders [26], conforming to the aircraft fuselage with hemi-spherical or hemi-ellipsoidal endcaps. This kind of geometry is not only highly parametrizable and scalable, but offers considerable advantages in manufacturability and modularity [27].

Larger components are preferable, as surface area increases with the square of the characteristic dimension, whereas volume, and thus the amount of stored fuel, grows with its cube. As part of the design space exploration performed in this paper, a consistent fuel tank theoretical capacity of $V_{\text{tank}} = 100\,\text{m}^3$ is assumed as suggested in Ref. [28], corresponding to $7850\,\text{kg}$ of LH_2 at the design storage temperature and pressure. This value not only reflects the energy demands of medium- to long-range next-generation aircraft [8], but is also compatible with the conceptual design proposed in Ref. [29], which is later taken as the reference platform for system integration. Moreover, realistic features necessary for tank integration are considered so to account for potentially detrimental integration effects. To interface the inner cavity with the aircraft's fuel system, the tank is equipped with two axial cutouts, whose dimensions – detailed in Section 3.4 – are selected to accommodate cryogenic fuel lines, while, to mitigate fuel displacement during vehicle manoeuvres, anti-sloshing baffles are introduced in Section 3.5.

2.1.2. The passively-insulated layered architecture

As previously noted, hydrogen, to remain in its liquid state, demands temperatures not exceeding $20.3\,\text{K}$, thereby necessitating thermal insulation which, to be efficient, should be embedded in the vessel design from the conceptual stage.

The use of insulating foam is identified by Brewer et al. [30] as the most efficient thermal management approach from a mass, safety, and maintenance standpoint. However, since spray-on foam insulation (SOFI) typically lacks adequate rigidity to be used on its own [31] and is highly susceptible to corrosion, a protective liner and a structural layer are required. Thus, the *passively-insulated cryogenic sandwich-composite architecture* [32], schematized in Fig. 1, is identified as a possible solution, which minimizes the number and mass of subsystems required for operation while reuniting in the same structure: (*i*) a liner, required for H_2 containment; (*ii*) a low density, low conductivity, low diffusivity insulation material that allows for dimensional variations; (*iii*) an outer structural shell.

The liner is typically constructed from either light-weight polymers or high-strength metallic alloys. For this study, a specific aluminium–copper alloy, the Al 2219-T8, is selected due to its favourable combination of low density, excellent cryogenic performance, corrosion resistance, and cost-effectiveness [33]. This alloy undergoes heat treatment, cold working, and artificial ageing to achieve the desired properties [34,35], making its susceptibility to embrittlement due to H_2-induced corrosion negligible [36].

Thermoset polyurethane (PUR) foam is commonly used as a core material in sandwich structures, featuring a thickness significantly greater than that of the outer layers. Its past applications in aerospace cryogenic tanks – most notably in the external tank of the Space Shuttle – underscore its effectiveness as a reliable yet simple heat barrier [37], simultaneously offering highly tailorable insulation properties through spray-on deposition techniques allowing for straightforward thickness management [38]. Given its importance in the aerospace industry, extensive thermo-mechanical characterization of this material is available [39,40], enabling the inclusion of temperature dependant thermo-mechanical properties in the finite-element modelling stage.

As it will be discussed further later in this work, without additional reinforcements, Al 2219-T8 is not a suitable choice for the construction of the outer structural tank layer [22]. To fulfil this role, a material yielding higher mechanical properties must be considered. Accordingly, two distinct and mutually exclusive alternatives are evaluated: either high-strength metallic alloy or a fibre-reinforced composite shell. The titanium alloy Ti-6Al-4V is first considered because of its superior specific strength and established use in the aerospace industry [41], with thermo-mechanical characteristics derived from Refs. [42,43]. The relevant constants for each of the above materials (liner, foam and metallic outer shell) are listed in Table 1.

The second candidate for outer shell construction is carbon fibre-reinforced plastic (CFRP). Although the use of composites in cryogenic applications is challenging due to the limited characterization of their behaviour at extremely low temperatures, several studies have demonstrated their feasibility and durability when properly integrated into multilayer architectures. Early investigations by Horiuchi and Ooi [44] showed that CFRPs retain high tensile strength at extremely low temperatures and long-term operation and vibration tests of cryogenic support structures confirmed no measurable degradation. Experimental studies have also clarified likely degradation mechanisms. For instance, Gates et al. [45] found that interfacial debonding in sandwich composites occurs primarily at the adhesive–core bondline, with fracture toughness increasing by about 20% at $4\,\text{K}$, suggesting improved resistance to delamination rather than embrittlement. Conversely, Islam et al. [46] emphasized that the marked thermal expansion coefficients mismatch between carbon fibres ($\approx -1\times10^{-6}\,\text{K}^{-1}$) and epoxy matrices ($\approx 50\times10^{-6}\,\text{K}^{-1}$) can induce stresses that promote matrix microcracking and resin embrittlement during cyclic operation. The study also highlighted how these effects can be mitigated through matrix toughening

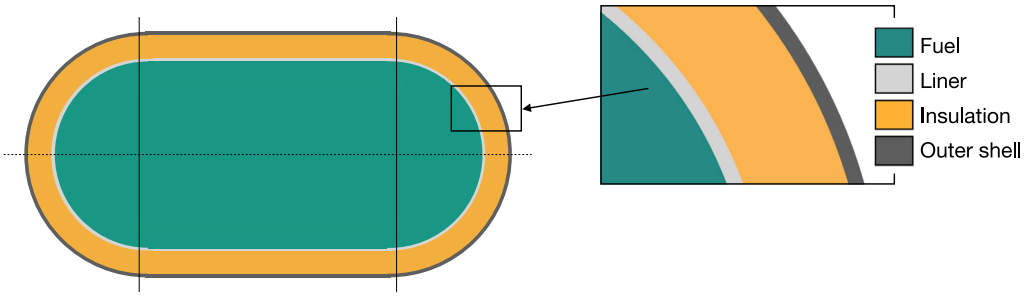

Fig. 1. Schematic of the insulated cryogenic sandwich architecture featuring a thin inner liner, an outer structural layer, and thick intermediate foam insulation.

Table 1
Mechanical and thermal properties of aluminium 2219-T8 alloy, unreinforced polyurethane PUR-96 foam, and Ti-6Al-4V alloy.

Property	Symbol	Aluminium	Polyurethane	Ti-6Al-4V	Units
Young's modulus	E	73.1	0.11	93.0	GPa
Poisson ratio	ν	0.33	0.3	0.34	–
Density	ρ	2840	96	4430	kg/m^3
Conductivity	κ	121	0.0163	6.7	$W\,m^{-1}\,K$
Specific heat capacity	C_p	864	1100	560	$J\,kg^{-1}\,K$
Thermal expansion coefficient	α	2.2×10^{-5}	30.9×10^{-6}	8.6×10^{-6}	K^{-1}
Yield strength	$\bar{\sigma}_y^{mat}$	500	2.25	1273	MPa
Reference temperature	T_{ref}	20	95	288	K

Table 2
Carbon fibre-reinforced plastic mechanical and thermal properties.

Property	Symbol	Value	Unit
Young's moduli	E_{11} $E_{22} \equiv E_{33}$	133 9.13	GPa
Poisson ratios	$\nu_{12} \equiv \nu_{13} \equiv \nu_{23}$	0.3	–
Shear moduli	$G_{12} \equiv G_{13} \equiv G_{23}$	5.2	GPa
Density	ρ	1600	kg/m^3
Conductivities	K_{11} $K_{22} \equiv K_{33}$	3.972 0.3363	W/mK
Specific heat capacity	C_p	1130.0	J/kgK
Thermal expansion coefficients	α_{11} $\alpha_{22} \equiv \alpha_{33}$	-0.2×10^{-6} 30×10^{-6}	1/K
Reference temperature	T_{ref}	288	K
Longitudinal Tensile Strength	X_t	2950	MPa
Longitudinal Compressive Strength	X_c	1570	MPa
Transverse Tensile Strength	Y_t	79	MPa
Transverse Compressive Strength	Y_c	190	MPa
Longitudinal shear strength	S_l	140	MPa
Transverse shear strength	S_t	88	MPa

and the inclusion of low thermal expansion coefficient or compliant interlayers, which suppress microcrack formation, improving interlaminar toughness at cryogenic temperature. Nonetheless, positioning the composite layer on the exterior side of the insulation, away from the cryogenic and potentially aggressive fuel, further mitigates such risks. The proposed multilayer architecture indeed keeps the composite shell close to ambient conditions, minimizing the exposure to extreme temperatures and the related thermal loads, while physically keeping H_2 separated from CFRP. Additionally, the presence of the metallic inner liner further mitigates the risk of the fuel permeation with potentially hazardous outcomes. Hence the use of composite material in the tank layout is modelled with individual ply properties of CFRP extracted from Refs. [28,47] and reported in Table 2.

2.2. Figures of merit

As anticipated, profound layout differences between H_2 and kerosene-powered vehicles stem from hydrogen's peculiar properties. Notably, as reported in Table 3, because of the far lower volumetric energy density of LH_2 when compared to conventional aviation fossil fuel, specific storage solutions are necessary.

Table 3
Comparison between kerosene and liquid hydrogen properties.

Property	Jet A-1	Liquid hydrogen	Units
Volumetric energy density	33	10.1	MJ/L
Gravimetric energy density	43.2	120	MJ/kg
Storage temperature	ambient	20	K

The integration of hydrogen tanks into feasible aircraft layouts is typically accompanied by mass penalties quantified by the *gravimetric efficiency* (η_{tank}), also known as the *gravimetric index*:

$$\eta_{tank} = \frac{W_{H_2}}{W_{H_2} + W_{tank} + W_{subsystems}}, \quad (1)$$

where W_{H_2} is the weight of the hydrogen the tank can store at design conditions, W_{tank} represents the structural weight of the tank itself and $W_{subsystems}$ quantifies the weight of the subsystems necessary for tank operation, which, given their simplicity, is assumed as 0 in the case of passive components. The gravimetric efficiency is a measure of the undesired effects associated with the use of specialized storage systems over simpler and highly-optimized aircraft jet fuel tanks. An increase in η_{tank} directly reduces the overall energy demand of the H_2-powered

airplane, having a system-level influence on both feasibility and competitiveness. Notably, as highlighted by Adler et al. [8], a threshold η_{tank} of $\approx$ 55% is identified, beyond which hydrogen-fuelled aircraft overall energy consumption is projected to be lower than current fossil fuel-based counterparts, hence, as the tank efficiency increases, range improves over conventional kerosene aircraft.

Besides increased mass, LH_2 storage poses an additional challenge: practical insulation limits heat transfer from the ambient to the cryogenic liquid inside the tank but does not eliminate it completely. In the *autogenous pressurization* mechanism, the evaporated fuel generated by heat ingress, must be vented to prevent exceeding the tank's structural limits. Thus, to assess the vessel thermal performance the fuel *boil-off rate* (BOR) is used being defined as

$$\text{BOR} = \frac{Q}{\rho_{\text{LH}_2} V_{\text{LH}_2} \lambda_{v_{\text{LH}_2}}}, \tag{2}$$

where Q represents the total heat flux from the exterior environment to the tank inner cavity, ρ_{LH_2} is the density of the liquid fuel, V_{LH_2} is the volume of LH_2 inside the tank and $\lambda_{v_{\text{LH}_2}}$ denotes the latent heat of vaporization for liquid hydrogen. In layered architectures, like the one schematized in Fig. 1, the global wall thermal resistance (R_{th}) can be approximated, exploiting the electrical analogy, as

$$R_{\text{th}} = \sum_i \frac{t_i}{\kappa_i \cdot S_i} \qquad i \in \{\text{Liner, Insulation, Outer shell}\} \tag{3}$$

where t_i is the thickness of the *i-th* layer, κ_i quantifies the thermal conductivity of the material constituting that layer, and S_i is the surface of the layer from which heat flows. Total heat flux can be therefore estimated as $Q = \Delta T / R_{\text{th}}$ which allows computing the BOR through Eq. (2). The instantaneous boil-off rate is not constant, rather it evolves as the mission progresses and fuel is consumed, exhibiting a quadratic increase with decreasing filling ratios [48]. Thus, the boil-off rate associated with the full tank is identified as a consistent metric for comparing the thermal performance of different designs. Such benchmark avoids misleading comparisons between partially filled and fully filled configurations. Future work will extend the framework to consider the effects of fuel consumption, enabling mission-dependent transient analysis. As a design requirement a daily allowable BOR = 2.50% of the stored LH_2 mass – corresponding to 8.18 kg/h – is adopted throughout the study as this value is identified by Mital et al. [49] as a both technologically and commercially viable compromise suitable to enable practical storage systems energy densities for airborne applications.

2.3. Computational model

2.3.1. Thermo-mechanical loads and boundary conditions

The FE tank model – evolved from Ref. [48] –, being conceived to reproduce a non-integral component, considers the tank exterior surface in contact with pressurized air inside the fuselage at the controlled temperature of $T_{\text{fus}} = 283$ K, consistent with the minimum achievable value from environmental control systems of commercial airliners [50], which should be set to minimize the ΔT. The external wall temperature (T_{ext}) is treated as an unknown variable in the thermal formulation, with natural convection assumed to occur in the surrounding ambient. The steady-state thermal–mechanical coupling adopted reflects the quasi-static conditions expected during cruise, where boundary temperatures vary slowly compared with the characteristic thermal diffusion time of the tank wall. Hence, under these assumptions, the convective heat flux at the tank wall (HFL_{ext}) is related to the temperature difference by:

$$\text{HFL}_{ext} = h_c^{\text{ext}} \left(T_{\text{fus}} - T_{\text{ext}} \right), \tag{4}$$

where h_c^{ext} is the external convective heat transfer coefficient, assumed to be 10 $\text{W/m}^2\text{K}$, consistent with the value adopted in Ref. [28]. Each material thermal conductivity influences the temperature distribution through the multi-layered wall, resulting in heat transfer driven by the temperature gradient between the external environment and the cryogenic fluid. While practical tank filling conditions do not exceed $\sim$ 97%, in an effort to simplify the model, the whole inner cavity is assumed full of LH_2 at the temperature of 20 K which, given the high thermal conductivity of the metallic liner, is the same temperature assigned to the inner layer internal surface. The presence of localized geometric discontinuities, such as refuelling ports or feed-line cut-outs, introduces additional conductive paths that can locally increase the heat flux through the insulation. In the absence of detailed geometric or experimental data applicable to these regions, a thermal-bridge correction, derived from Ref. [51], is applied in the tank models featuring such additions, by amplifying the insulation-averaged heat-flux magnitude by 50%. This assumption is adopted to approximate the thermal penalty likely associated with metallic reinforcements and partial insulation of the feed-lines. However, it should be noted that such correction constitutes a simplified representation of the thermal penalty associated with geometric discontinuities and likely provides a lower-bound estimate. In practical configurations, solid conduction through metallic feed lines, structural reinforcements, and partially insulated interfaces can introduce preferential heat-transfer paths that may exceed the magnitude of the penalty adopted here. A rigorous quantification of these effects would require detailed geometric modelling of the cutouts and dedicated cryogenic experimental measurements. Accordingly, the present correction is intended to capture the first-order influence of thermal bridging, recognizing that higher-fidelity assessments would benefit from interface-specific thermal characterization.

From a mechanical standpoint, the vessel is pressurized to maintain a pressure differential of $\Delta p = 1.7$ bar, selected to prevent ambient air ingestion and facilitate fuel flow. Additionally, since the analysis is assumed to be performed at 1 G, the stored fluid exerts hydrostatic pressure over the inner tank surface. Mechanical boundary conditions are modelled to replicate practical tank-airframe integration strategies. A constraint layout inspired by the H2FLY demonstrator [52] is adopted, in which the vessel, whose longitudinal axis is aligned with that of the fuselage, is supported along three circular edges on the outer layer. These constrained edges are located at the intersections between the end-domes and the cylindrical section, as well as at the midpoint of the cylindrical body and restrain motion in all translational and rotational degrees of freedom.

2.3.2. Finite-element simulation

The multi-physics model is reproduced in Abaqus/CAE [53] by means of multi-parametric Python scripts so to ensure robustness and flexibility. The vessel employs two three-dimensional shell revolution entities, representative of the internal liner and outer structural layer – whose sections are assigned with geometrically consistent offset – and a middle solid domain whose thickness is two orders of magnitude greater than the other two layers. The anti-sloshing baffles are modelled as independent planar shell parts and subsequently connected to the revolution shell liner through a merging operation. Dedicated partitions are introduced to ensure node coincidence at the interface between the liner and baffles, resulting in a conformal mesh that enforces displacement continuity. The bulkheads are thus mechanically attached to the inner surface of the liner along their external perimeter through coincident nodes. Each of these parts, complete with realistic elements, is shown in Fig. 2. A coupled thermo-elastic steady-state analysis is performed to evaluate tank behaviour under prolonged operating conditions, as the structure is subjected to severe temperature gradients caused by cryogenic storage. The analysis step is defined considering a separated solution where the thermal field and mechanical equilibrium are solved sequentially within each increment, allowing efficient convergence while maintaining full coupling through temperature-dependent material properties and thermal strains. A maximum of 100 increments is allowed, with an initial unitary increment size. Non-linear geometric effects are deactivated as

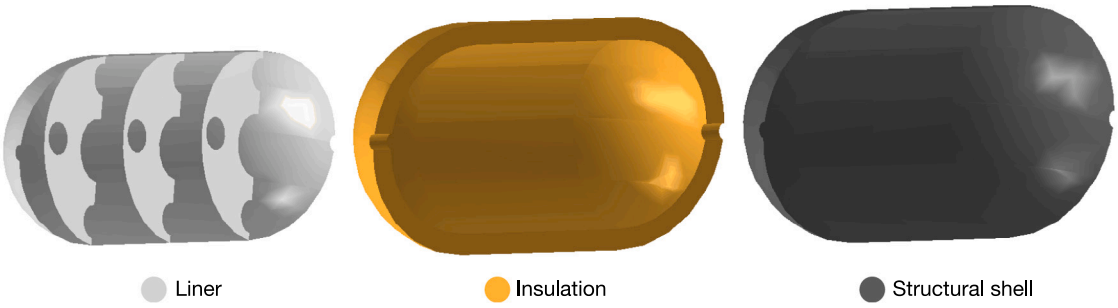

Fig. 2. Exploded representation of the three finite-element entities constituting the pressure vessel featuring hemi-spherical domes, axial cutouts and three anti-sloshing baffles.

the expected deformations are small compared to the component characteristic dimension. The analysis iterates using the Newton–Raphson method until the equilibrium residuals (forces, moments, heat fluxes) are below 5.0×10^{-3} and the variable corrections (displacement, rotation, temperature) are below 1.0×10^{-2}. Step convergence occurs in two equilibrium iterations with no cutbacks, and no divergence warnings recorded. Hence, each of the tank layers is meshed using elements with both temperature and displacement degrees of freedom (DoF), namely S3RT and S4RT elements with reduced integration for the shell entities, and C3D8T eight-node continuum thermally coupled bricks for the solid part. These element types are selected with the intent of balancing accuracy and computational cost. Reduced-integration S4RT shell elements are used for the inner and outer thin layers to mitigate shear locking and reduce times. Similarly, S3RT elements discretize the anti-sloshing baffles. Conversely, fully integrated C3D8T elements are adopted for the thick polyurethane insulation instead of reduced-integration C3D8RT elements, which are known to exhibit bending instabilities and severe hourglassing without appropriate control [53–55]. The C3D8T formulation provides improved stress and displacement accuracy near interfaces and regions with strong gradients, making it indicated for coupled thermo-mechanical simulations. Nevertheless, for preliminary design phases and large parametric studies, reduced-integration elements may employed to build lower-fidelity models with significantly lower computational cost. Mesh convergence is verified by successive refinements, evaluating both scalar outputs and field distributions. Particular attention is given to the spatial distribution of stress, heat-flux per unit area, and temperature as well as their respective through-the-thickness profiles. The mesh is considered converged when further refinement produce no appreciable change in these distributions, confirming grid-independent results for the quantities of interest. Results of the convergence study are reported in Fig. 3 and a number of DoF equal to 3.6×10^5 is ultimately selected. For generality, the plot x-axis is expressed in non-dimensional form as the ratio between the position across the foam layer thickness (χ_{PUR}) and a reference insulation thickness ($t_{\mathrm{PUR_{ref}}}$).

2.3.3. Material failure criteria

Assuming ε_{kl} as the total strain tensor and α_{kl} as the thermal expansion tensor, the tank is sized to ensure that the thermo-mechanical stress, $\sigma_{ij} = C_{ijkl}\left(\varepsilon_{kl} - \Delta T \alpha_{kl}\right)$, always remains below the allowable limit in each layer of the sandwich structure. Hence, material failure is assessed via layer-specific criteria. For isotropic materials (metals and foam), the *von Mises* equivalent stress criterion is used:

$$\sigma_{eq} = \sqrt{\frac{1}{2}[(\sigma_1 - \sigma_2)^2 + (\sigma_2 - \sigma_3)^2 + (\sigma_3 - \sigma_1)^2]} < \bar{\sigma}_y^{\mathrm{mat}}, \tag{5}$$

with $\sigma_1, \sigma_2, \sigma_3$ the principal stresses and $\bar{\sigma}_y^{\mathrm{mat}}$ the material yield strength. At the same time, to assess damage onset in the orthotropic layer the *Hashin criterion* (HSNCRT) is applied, distinguishing between the fibre and matrix damage initiation modes:

$$\text{Fibres} \quad \begin{cases} \left(\frac{\sigma_{11}}{X_T}\right)^2 \le 1 & Tension \\ \left(\frac{\sigma_{11}}{X_C}\right)^2 \le 1 & Compression \end{cases} \tag{6}$$

$$\text{Matrix} \quad \begin{cases} \left(\frac{\sigma_{22}}{Y_T}\right)^2 + \left(\frac{\sigma_{12}}{S_L}\right)^2 \le 1 & Tension \\ \left(\frac{\sigma_{22}}{2S_L}\right)^2 + \left[\left(\frac{Y_C}{2S_T}\right)^2 - 1\right]\frac{\sigma_{22}}{Y_C} + \left(\frac{\sigma_{12}}{S_L}\right)^2 \le 1 & Compression \end{cases} \tag{7}$$

where $X_{T,C}$, $Y_{T,C}$, $S_{L,T}$ are the respective strength parameters, and σ_{11}, σ_{22}, σ_{12} are the stresses in the local material frame. Additionally, in compliance with current commercial aviation standards, a uniform safety factor of SF = 1.5 is retrieved from FAR§25.303 [56] and explicitly embedded into the optimization algorithm so that the feasible design space directly reflects the certified structural margins. Accordingly, adjusted material failure thresholds become: $\bar{\sigma}_{\mathrm{SF}}^{\mathrm{Al}} = 333\,\mathrm{MPa}$, $\bar{\sigma}_{\mathrm{SF}}^{\mathrm{PUR}} = 1.5\,\mathrm{MPa}$, $\bar{\sigma}_{\mathrm{SF}}^{\mathrm{Ti}} = 849\,\mathrm{MPa}$, $\mathrm{HSNCRT}_{\mathrm{SF}} = 0.667$.

2.3.4. Finite-element model validation

The temperature distribution predicted by the present finite-element model is consistent with the reference study by Mantzaroudis et al. [28], both in terms of gradients and overall magnitude, although a root mean square error (RMSE) of 9.29 K, corresponding to a maximum deviation of approximately 15%, is observed along selected paths, as reported in Fig. 4. This discrepancy likely arises from the combined influence of modelling assumptions and input-data uncertainties. In particular, differences in mesh topology, implementation of thermal boundary conditions, and temperature-dependent thermal properties can significantly affect the local heat-flux gradients and wall temperatures. In addition, the limited availability of open-access experimental data for full-scale cryogenic vessel – probably due to proprietary constraints and high commercial value of such systems – hinders precise calibration of numerical parameters for physical tests. Consequently, the present validation should be interpreted as a numerical cross-comparison, rather than an absolute experimental benchmark. A further implication of the observed discrepancy is that the slightly lower insulation temperatures predicted by the present model imply a reduced heat-leak estimate and therefore a potentially non-conservative boil-off rate. The actual thermal loads acting on the tank, however, depend strongly on unknowns such as the aircraft mission profile, design cruising altitude, ambient temperature, dormancy times, and ground turnaround operations. A fully conservative assessment would therefore require more detailed transient and mission-specific thermal modelling. These aspects lie beyond the scope of the present validation but motivate future work aimed at refining the accuracy and robustness of the storage-system design. Nonetheless, within these bounds, the agreement obtained supports the adequacy of the adopted modelling strategy for thermo-mechanical design and optimization of liquid-hydrogen storage tanks.

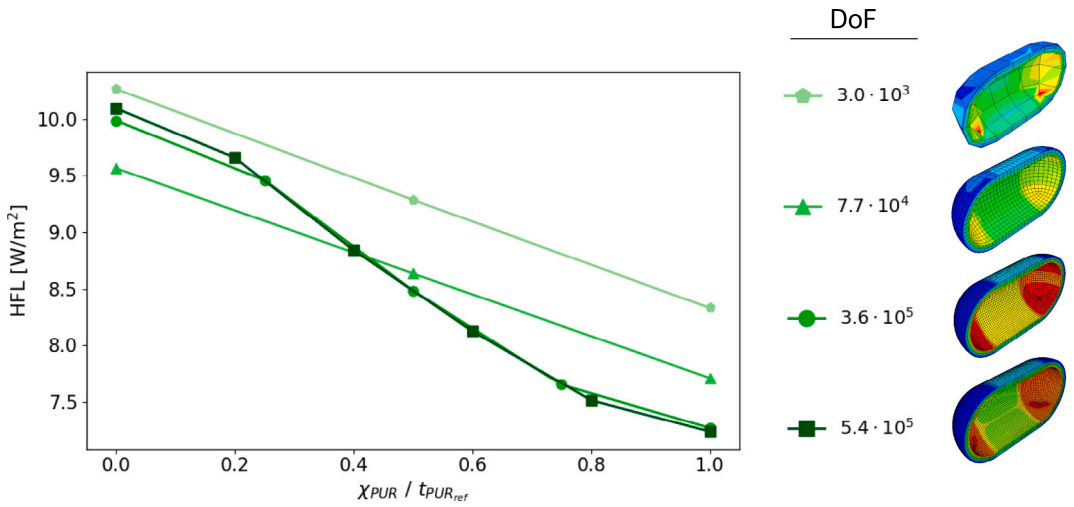

Fig. 3. Mesh convergence study showing the profiles of heat flux per unit area (HFL) measured at the endcap apex across the normalized insulation thickness ($\chi_{PUR}/t_{PUR_{ref}}$) for increasing degrees of freedom (DoF). The right column illustrates the corresponding domain discretization and variable distribution at different levels of refinement.

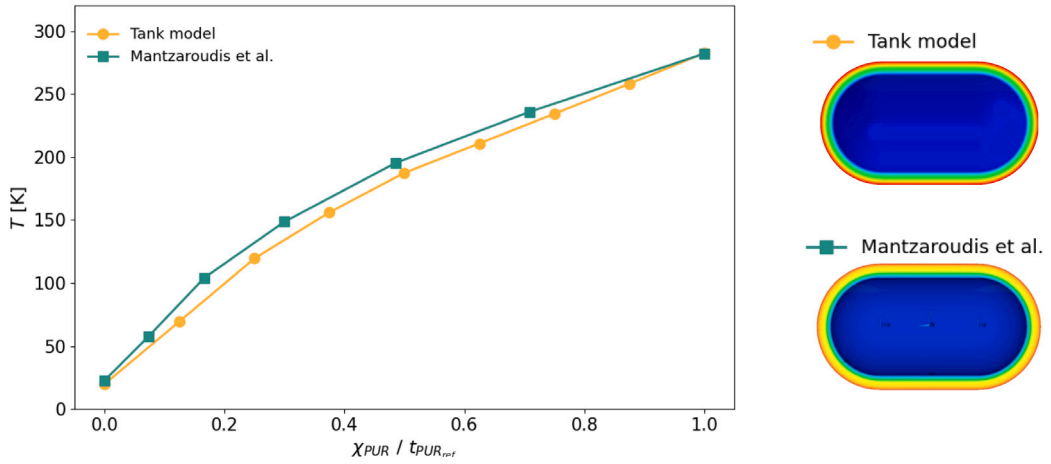

Fig. 4. Validation of the thermo-mechanical FE model by comparison of both magnitude and spatial variable distribution - in this case absolute temperature - across the normalized insulation thickness for the tank model developed in this study and the one proposed by Ref. [28].

2.4. Optimization problem formulation and workflow integration

The optimization problem statement, reported in Eq. (8), aims to minimize the tank mass (m_{tank}) with respect to the vector of design variables (t_j), subject to inequality constraints (g_i) and bound constraints ($t_j^{\text{lb}}, t_j^{\text{ub}}$)

$$\begin{aligned}
&\texttt{minimize} && m_{\text{tank}}(t_j)\\
&\texttt{withrespectto} && t_j^{\text{lb}} \le t_j = [t_{\text{Al}}, t_{\text{PUR}}, t_{\text{Ti}}, t_{\text{CFRP}}] \le t_j^{\text{ub}}\\
&\texttt{subjectto} && g_i = \begin{cases} \dfrac{\sigma_{\text{Al}}}{\tilde{\sigma}_{\text{SF}}^{\text{Al}}} - 1 \le 0 \\ \dfrac{\sigma_{\text{PUR}}}{\tilde{\sigma}_{\text{SF}}^{\text{PUR}}} - 1 \le 0 \\ \dfrac{\sigma_{\text{Ti}}}{\tilde{\sigma}_{\text{SF}}^{\text{Ti}}} - 1 \le 0 \\ \text{HSNCRT}_{\text{SF}} - 0.667 \le 0 \\ \text{BOR} - \text{BOR}_{\text{allowable}} \le 0 \end{cases}
\end{aligned} \tag{8}$$

where only one of the two constraints – either titanium yielding or composite damage initiation – is applied at a time, since the outer structural layer construction is evaluated using one material or the other in each configuration, as detailed in Section 3. Accordingly, the outer-layer strength constraint is strictly configuration-dependent: titanium architectures activate only the yield-based inequality, whereas composite architectures activate only the Hashin damage criterion, with the two formulations remaining mutually exclusive within the optimization. The *Interior-Point method* is used by MATLAB's [57] `fmincon` function to reformulate the constrained problem into a sequence of unconstrained problems using a logarithmic barrier function. To ensure the constraints are never violated, the method adds a logarithmic barrier function to the objective

$$F(t_j) = f(t_j) - \mu \sum_{j=1}^{N} \log(-g_i(t_j)), \tag{9}$$

where μ is a positive barrier parameter decreasing at each iteration, while the term $-\log(-g_i(t_j))$ forces the constraints to remain negative, becoming large when $g_i(t_j)$ approaches zero, forcing the algorithm to stay inside the feasible region. As $\mu \to 0$ the solution approaches the constrained optimum. Upper and lower bounds constraints are enforced by adding $-\log(t_j - t_j^{\text{lb}}) - \log(t_j^{\text{ub}} - t_j)$ to the objective function, ensuring that t_j never reaches its bounds. Thus, the modified problem solved at

Table 4
Lower and upper thickness bounds for each material considered in the LH_2 vessel architecture.

	Al 2219-T8	PUR-96	Ti-6Al-4V	$CFRP_{ply}$	Unit
t^{lb}	0.5	25	3	0.125	mm
t^{ub}	10	950	50	10	mm

each iteration is

$$\min f(t_j) + \mu \sum_{j=1}^{N} \log(-g_i(t_j)) + \sum_{j=1}^{N} (-\log(t_j - t_j^{lb}) - \log(t_j^{ub} - t_j)). \tag{10}$$

At each step, the optimizer approximates gradients using *finite differences* as

$$\frac{\partial f}{\partial t_j} \approx \frac{f(t_j + h) - f(t_j)}{h}. \tag{11}$$

The direction of movement is found trough the Newton system

$$H(t)\Delta t = -\nabla F(t), \tag{12}$$

where $H(t)$ is the Hessian matrix describing how the function curves, Δt is the step size and $\nabla F(t)$ is the gradient describing the function slope. Since the computation of the exact Hessian matrix is computationally expensive, `fmincon` approximates it using the quasi-Newton BFGS approximation equation, updating H_{k+1} as

$$H_{k+1} = H_k + \frac{y_k y_k^T}{y_k^T s_k} - \frac{H_k s_k s_k^T H_k}{s_k^T H_k s_k}, \tag{13}$$

where $s_k = t_{k+1} - t_k$ is the step vector quantifying the change in the design variables, while $y_k = \nabla f_{k+1} - \nabla f_k$ measures the change of the gradient of the objective function between consecutive iterations. The algorithm stops when:

- The first-order optimality is small, meaning that gradients are close to zero, therefore in the vicinity of a minimum, $\|\nabla f(t) < \epsilon\|$;
- The step size $\|\Delta t\|$ is small;
- Constraint violations $g_i(t) \leq 0$ are within tolerance.

As common in structural optimization, given the large number of constraints, an aggregation method is used to limit the increase in computational cost and improve the convergence behaviour. Thus, the Kreisselmeier–Steinhauser aggregation function [58] is implemented to represent a conservative estimate of the maximum of all constraints at any point in the design space as

$$\mathrm{KS}(t) = \frac{1}{\rho_{ag}} \ln\left(\sum_{i}^{N} e^{\rho_{ag} g_i(t)}\right), \tag{14}$$

where $\rho_{ag} = 100$ is the aggregation parameter, chosen after several tries, quantifying how closely the KS function approximates the maximum of the constraint functions.

The use of finite-difference approximations for derivative evaluation introduces the step-size dilemma, which aims to balance truncation and round-off errors. Hence, a sensitivity study on the step length is conducted considering the following output quantities: equivalent stress in the liner and insulating layer; heat flux per unit area in the insulating layer; and Hashin index in the outer shell. The analysis demonstrates that a step size of $\Delta t = 1.0 \times 10^{-5}$ m represents a suitable choice.

Given that one of the main objectives of this study is to optimize the design of LH_2 tanks through their layer thicknesses, practical lower and upper bounds -t^{lb} and t^{ub} respectively- must be defined. These bounds are primarily based on technological considerations and are reported in Table 4.

While, as later outlined, the metallic liner indeed contributes to the tank overall mechanical behaviour, its primary function is as a containment layer to prevent fuel permeation and protect other elements from corrosion. Thus, as it will be highlighted by the optimized tanks architectures in Section 3, t_{Al} will assume values close to t_{Al}^{lb}, in the order of 0.5 mm [59]. Such thin-gauge metallic components can be manufactured with controlled defect levels through hydroforming processes, which are particularly well-suited for producing water-tight geometries as those required in pressure vessel applications, whose layer thickness, however, should not exceed 10 mm [60]. The polyurethane insulation layer, by contrast, is expected to be an order of magnitude thicker than the inner liner, requiring dimensions achievable with relatively straightforward spray-on technology. While t_{PUR}^{lb} is derived from the work of Fesmire et al. [38], given the high degree of process adaptability, the upper bound is defined based on previous studies on foam-insulated H_2 cryogenic tanks, identifying in ≈ 950 mm a pragmatic limit associated to excessive mass and dimensions incompatible with most aircraft designs [48]. Ti-6Al-4V thickness, hereafter denoted as t_{Ti} for conciseness, is assumed to have a practical lower bound around 3 mm [61], limited by manufacturing methods that may involve conventional forming and joining operations or metal additive manufacturing technologies [62]. Finally, in accordance with Ref. [63], the lower bound for individual composite plies is set to 0.15 mm, given that thinner plies may induce compatibility issues with automated fibre placement processes [64], necessary for efficient composite tailoring and manufacturing. The composite outer shell is modelled with a stacking sequence of eight plies, with the number of plies kept constant regardless of their orientation. The thickness of each ply is defined as a design variable in the optimization, thereby determining the total thickness of the shell. Consequently, the laminate thickness varies as a function of ply thickness. Variations in tank performance across different stacking sequences are evaluated, enabling the identification of an optimum lamination strategy.

Optimization convergence is reached when the first-order optimality falls below 1.0×10^{-3} and all constraint violations are $< 1.0 \times 10^{-3}$. Step updates with amplitudes below 1.0×10^{-5} are considered numerically insignificant and trigger termination, if the other criteria are satisfied. Central finite differences with minimum and maximum perturbations of 1.0×10^{-4} and 1.0×10^{-3} respectively, are used as gradients approximation. For the representative case of the ellipsoidal composite tank model complete with refuelling cutouts and anti-sloshing bulkheads, the algorithm converges in 16 iterations and 195 function evaluations, reaching a first-order optimality measure of 6.0×10^{-4} and zero constraint violation. Each function evaluation triggers a full thermo-mechanical analysis. On the employed 32-core workstation, a single evaluation required approximately 40 s of wall time, corresponding to a total computational cost of $\approx$ 2 h of serial wall time. The framework is indeed parallelizable across multiple cores or nodes, which reduces turnaround according to available resources.

The optimization formulation is coupled with the finite-element analysis stage, resulting in the integrated computational framework schematized in Fig. 5. Material definition, component geometry, thermal and mechanical boundary conditions are all adjustable to reproduce the operating environment and high-level requirements. These data are then integrated into the Python/Abaqus code which reads the layers thicknesses from an input file and creates the FE model launching the simulation. Once the analysis is complete, a post-processing stage extracts relevant output from the result file and imports it into the MATLAB environment. Here, the optimization algorithm determines the next set of layer thicknesses, which are fed back into the Python script for the subsequent iteration. The process continues until stopping criteria are met, at which point the optimization is considered concluded, and the optimum set of design variables and FE results are available.

To further enhance the tank design through mass reduction, the optimization framework allows for distinct thickness assignments between the cylindrical section and the hemi-spherical or hemi-ellipsoidal endcaps of each structural layer. This choice accounts for thin-walled

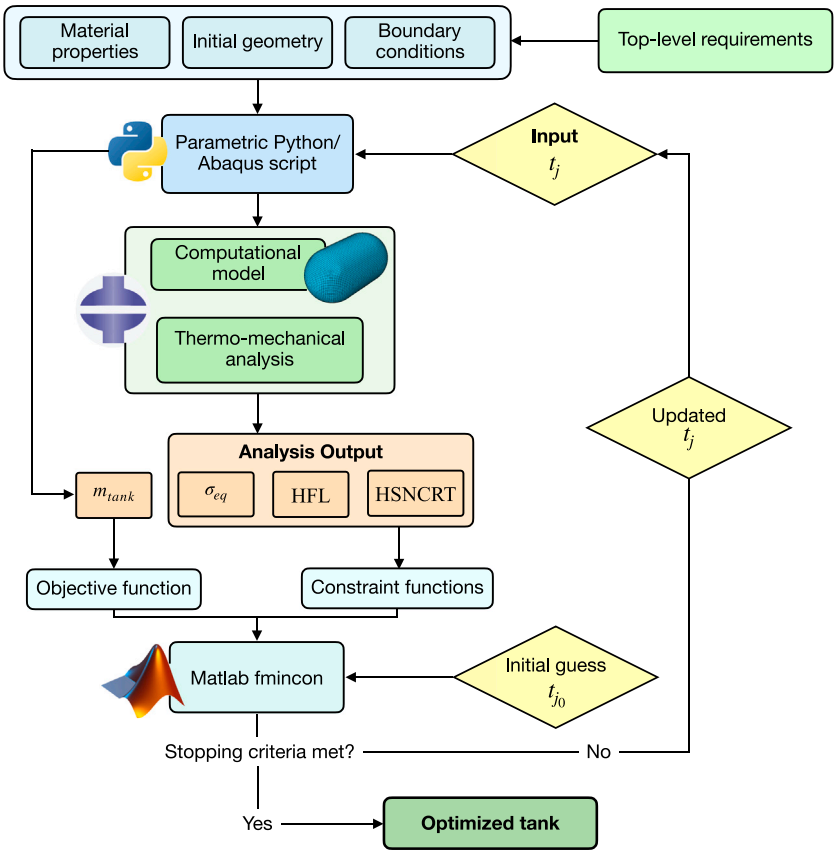

Fig. 5. Block diagram representing the optimization logic. Design variables are fed into the FE model and solver and, based on resulting metrics and residuals, the optimization algorithm iteratively updates the design variables until convergence criteria are satisfied.

pressure vessel theory, which states that, under simplified assumptions, the tangential stress in a spherical shell is approximately half the circumferential stress in a cylindrical shell of the same radius. Consequently, different geometries require different optimal thicknesses. The framework supports further discretization of the structural layers into patches, with each patch thickness treated as an independent design variable. Increasing the number of patches expands the dimensionality of the design space, enabling more refined thickness distributions and, consequently, enhanced structural tailoring.

2.4.1. Optimization loop validation

The optimization framework is validated through a dedicated study in which the tank geometry – specifically its aspect ratio $\phi = L/R$, where L denotes the length of the cylindrical section and R the radius of the hemispherical endcaps – is treated as a design variable. For a fixed capacity and prescribed thermo-mechanical conditions, the algorithm is allowed to change the shape of the vessel. To retain a consistent compromise between computational cost and numerical accuracy when the tank dimensions vary, a constant ratio between the characteristic mesh seed size and the reference tank dimension is enforced. As discussed in Section 2.1.1, in absence of shape- and integration-related constraints, optimal performance is achieved by a spherical tank, which minimizes the surface-to-volume ratio, consequently reducing heat ingress and insulation requirements. Accordingly, starting from an arbitrary initial guess of $\phi = 3.5$ – i.e. a cylindrical vessel with its length three and a half times the radius – the optimizer indeed converges towards $\phi_{\text{opt}} = 0$. The evolution of the tank geometry from the initial to the optimized configuration is illustrated in Fig. 6, highlighting that this result is valid strictly under the constant internal volume requirement.

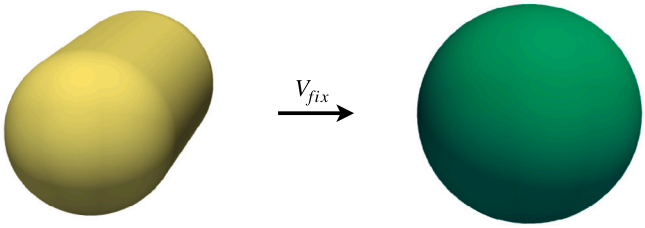

Fig. 6. Initial (yellow) and optimized (green) vessel shapes resulting from the optimization process where ϕ is treated as a design variable. Thermo-mechanical boundary conditions, material properties, and tank capacity are held constant throughout the analysis.

3. Optimized tank architectures comparison and layout integration

This section introduces the LH_2 vessel configurations investigated in the study, discusses each of the corresponding optimized mass distribution, along with fuel mass fraction, and provides a results comparison, selecting the most representative tank layout which is then tailored to an advanced sustainable airframe to assess the thermo-mechanical fields.

Each architecture is defined by a specific set of geometric and design features, including dome shape, presence of cutouts, and internal baffles. As outlined in Section 2.1.1, fixed theoretical fuel capacity and BOR are enforced across all cases to ensure consistent comparison criteria. The geometric parameters defining each vessel – indexed using ascending Roman numerals (I to VI) – are reported in Table 5, with the associated variables referenced according to the schematics provided

Table 5
Summary of geometric parameters, layer composition and structural features for each tank configuration. Dimensions defining the internal cavity are reported for all vessels, while cutout and bulkhead openings diameters are specified only for configurations that incorporate such features.

	Parameter	I	II	III	IV	V	VI
Internal cavity [m]	L	4.24	4.24	5.32	4.24	4.24	5.32
	$R = a$	2.12	2.12	2.12	2.12	2.12	2.12
	b	–	–	1.32	–	–	1.32
Cutout [m]	D_{co}	–	–	–	0.15	0.15	0.15
Bulkhead [m]	D_{BH_c}	–	–	–	–	1.40	1.40
	D_{BH_r}	–	–	–	–	0.37	0.37
Material	Inner	Al2219-T8					
	Middle	PUR-96					
	Outer	Ti-6Al-4V	CFRP	CFRP	CFRP	CFRP	CFRP
Feature	Domes	Hem.-sph.	Hem.-sph.	Hem.-ellip.	Hem.-sph.	Hem.-sph.	Hem.-ellip.
	Cutouts	–	–	–	Yes	Yes	Yes
	Bulkheads	–	–	–	–	Yes	Yes

in Fig. 7. In particular: L represents the length of the tank cylindrical region, R is the radius of the hemi-spherical endcap, which is assumed equal to the semimajor axis of the hemi-ellipsoidal dome a. The semiminor axis of the hemi-ellipsoidal endcap is denoted by b. D_{co} represents the diameter of the circular refuelling cutout. Anti-sloshing baffles are assumed as disks, with diameter R, on which five circular openings are made. These holes are defined by D_{BH_c} and D_{BH_r}, which respectively represent the diameter of the single central opening and the one of the four radial ones. The table also reports the material composition of each tank layer along with the main features.

3.1. Tank I — Reference metal vessel

As a baseline for comparison, a simple tank model with the external layer made by titanium alloy and featuring hemi-spherical endcaps is first analysed. The vessel architecture, schematized in Fig. 7*a*, employs Ti-6Al-4V for the structural layer, while the inner and middle layers adopt the same materials used in all other tank configurations, namely aluminium for the liner and foam for the insulation. The employment of the same alloy used for fuel containment is evaluated also for the construction of the outer shell, however, this solution proves unable to meet the mechanical constraints, leading to unacceptable safety margins throughout the entire range of design variables defined in Table 4. This outcome reflects a physical limitation rather than a numerical issue, as the optimizer could not identify a feasible configuration within the prescribed bounds and the safety-factor-adjusted constraints. The combination of moderate stiffness and relatively high thermal expansion of Al 2219-T8 results in significant thermally induced stresses in the outer layer, particularly under the steep temperature gradients acting across the tank wall and in the absence of additional reinforcements. In fact, while the alloy exhibits excellent strength at cryogenic temperatures, its properties degrade significantly as T increases [35], as occurs at the outer surface of the vessel where thermally induced stresses are highest. Even with increased thickness, the safety-factor-adjusted yielding threshold remains violated, indicating that an all-aluminium configuration would require uneconomically heavy sections to achieve acceptable safety margins. Hence, the use of the titanium alloy represents a feasible, albeit significantly more expensive compromise, with a specific market price nearly 17 times higher than that of aluminium [65,66].

Having defined the component architecture, the optimization results are summarized: the mass distribution of the all-metal vessel is presented in Fig. 7*b*, where the relatively thick and dense structural layer accounts for the majority of total mass, leading to a comparatively low gravimetric efficiency, around 30%. The thin liner constitutes merely 1.5% of m_{tank} while the quantity of insulation is primarily dictated by the thermal design requirements, which is a concern also in the other tank configurations.

3.2. Tank II — Reference composite vessel

While retaining Al 2219-T8 and PUR-96 for the inner and middle layers respectively, the tank layout schematized in Fig. 7*c* replaces Ti-6Al-4V with fibre-reinforced composite material for the outer shell construction. The *quasi-isotropic* stacking sequence assigned to the composite layer, similarly to Ref. [28], is $[0°/90°/45°/-45°]_S$ so to uncouple shear and extension deformations. As it will be shown in Section 3.6, this sequence yields the best results among other popular options, leading to the lowest overall component weight. Hence, it is adopted for all analyses detailed in this chapter unless otherwise specified. The optimized tank, which, at this stage, does not incorporate practical features such as cutouts or anti-sloshing baffles, exhibits a profoundly different mass distribution compared to the all-metal construction, as shown in Fig. 7*d*.

The use of a composite outer shell, compared to the metallic design of Section 3.1, proves remarkably effective: the structural layer mass is reduced by a factor of 13, and the inner liner, which despite being intended only as a protective layer indeed contributes to the mechanical behaviour of the tank, has its mass reduced by a factor of ≈ 2. Once again, the thickness of the insulating layer, mainly linked to the thermal behaviour, remains mostly unchanged. Overall, composite use results in a vessel whose total mass is reduced by 59% compared to the all-metal counterpart, translating into an improvement of 20.8% in absolute η_{tank}.

3.3. Tank III — Ellipsoidal composite vessel

Hemi-ellipsoidal domed pressure vessels appear to be preferred by the aerospace industry [52,67,68] due to their favourable balance between manufacturability and volumetric efficiency. This geometry indeed facilitates integration with surrounding elements, especially within fuselage-constrained environments. Therefore, to provide insight on the influence of dome shape over tank performance, hemi-ellipsoidal endcaps are implemented in the vessel design, as schematized in Fig. 7*e*. As reported by Gomez et al. [22], such domes achieve optimal weight and structural efficiency when the ratio between the ellipsoid semi-axes is $a/b = 1.6$, hence, this value is adopted in the design under investigation. For consistency with the reference hemi-spherical designs previously discussed, no cutouts or internal baffles are introduced at this stage. The implementation of hemi-ellipsoidal endcaps leads to increased surface area, responsible for increased heat inflow and yielding a slightly less effective stress distribution when compared to hemi-spherical domes, ultimately leading to mass penalty, Fig. 7*f*. In particular, liner mass increases by 12% to accommodate the reduced load-bearing capabilities and increased surface, while the structural layer exhibits an increase of approximately 8.5%. Moreover, the rise in vessel surface-to-volume ratio translates in slightly thicker insulation needed to maintain the design venting rate, ultimately determining an overall m_{tank} increase of 3.1% compared to Tank *II*, attributable solely to the change in tank shape.

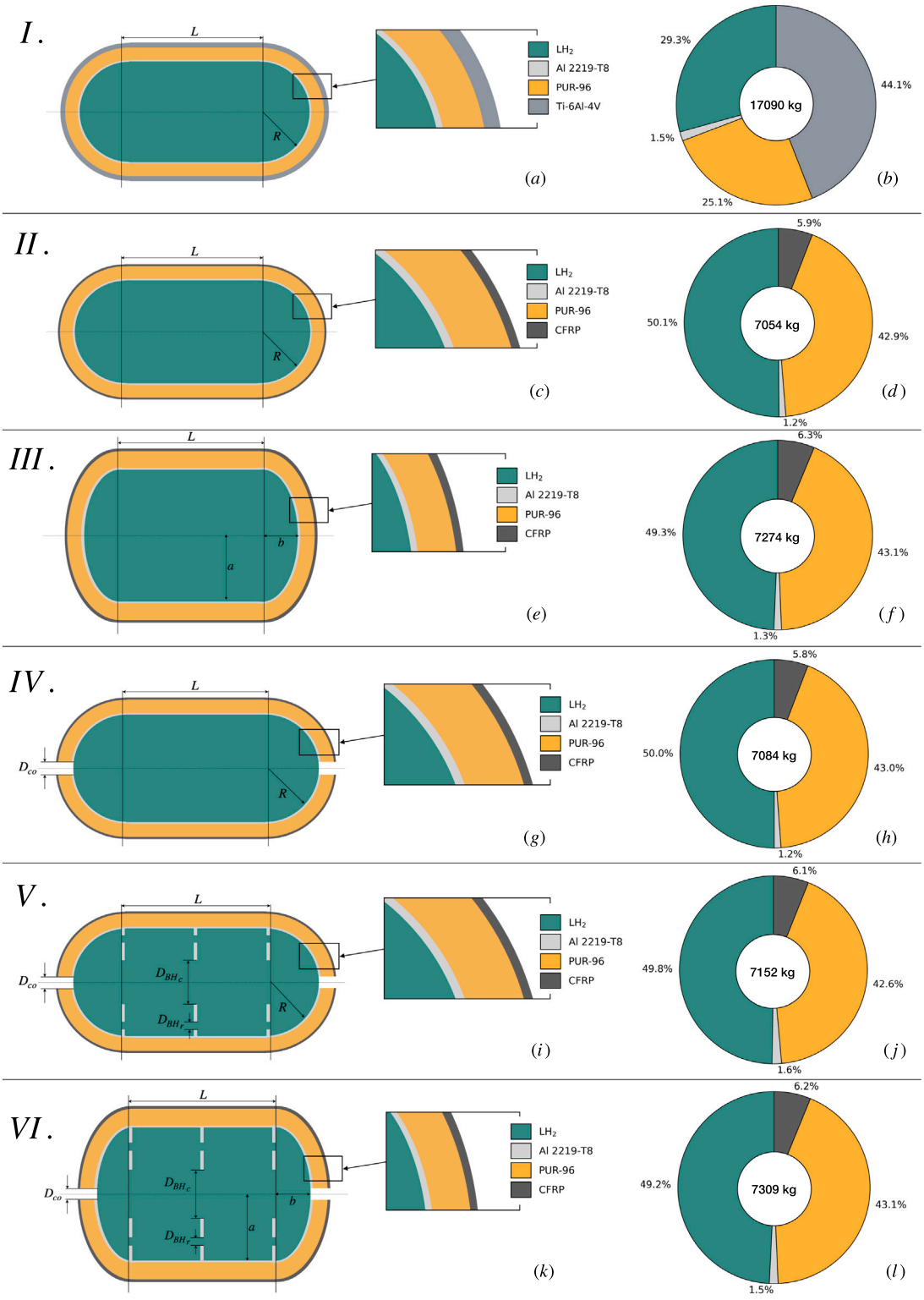

Fig. 7. Schematic representation of each vessel materials and geometry (*a, c, e, g, i, k*); optimized mass breakdown between fuel and constituting layers (*b, d, f, h, j, l*).

3.4. Tank IV — Composite vessel with refuelling cutouts

Cutouts to interface the tank cavity with fuel lines, sensors, and gas extraction pipes are now introduced in the tank layout. Given that the vessel is designed to be integrated within the aircraft fuselage, with its longitudinal axis aligned with that of the airframe, a practical placement for these openings is on the tank endcaps [69]. The cutout diameter, highlighted in Fig. 7*g*, is selected based on current commercial offerings of cryogenic liquid fuel lines [70]. To account for the potentially locally reduced insulation performance at the interface between the opening and external elements, a thermal penalty is introduced, following a methodology similar to the one proposed in Ref. [51]. The thermal model is thereby updated by the definition of an additional heat flux acting on the internal surface of the exposed

insulation, whose magnitude is equal to 50% of the average heat flux per unit area computed for the equivalent foam layer without cutouts. Consequently, to satisfy the prescribed boil-off rate constraint, a slight increase in insulation thickness is observed, resulting in a 0.6% gain in polyurethane mass compared to the reference tank discussed in Section 3.2. This outcome is reflected in Fig. 7*h*, which presents the mass distribution among the tank's layers and stored LH_2.

3.5. Tank V — Composite vessel with refuelling cutouts and anti-sloshing bulkheads

Further expanding the design space for onboard LH_2 pressure vessels, a configuration incorporating anti-sloshing internal baffles, alongside the cutouts introduced in the previous section is analysed, as schematized in Fig. 7*i*.

The geometry of the bulkheads is adapted from Ref. [71], with relevant geometric parameters listed in Table 5. The baffles are assumed to be manufactured from the same material as the metallic liner into which they are integrated and their thickness is controlled by the optimizer. As evidenced by the optimized tank weight distribution of Fig. 7*j*, the inclusion of anti-sloshing walls leads to significant increase in inner layer mass compared to the baffle-less tank. Specifically, the inclusion of such devices yields a 40% rise in m_{Al}. Nevertheless, since insulation and composite thicknesses remain largely unchanged, the overall tank mass increase is limited to approximately 1%.

3.6. Tank VI — Ellipsoidal composite vessel with refuelling cutouts and anti-sloshing bulkheads

The vessel layout detailed in the previous section is further evolved by the inclusion of hemi-ellipsoidal domes. This final configuration, reproduced in Fig. 7*k*, incorporates all the pragmatic features considered throughout this study and it is therefore regarded as the most representative design among the investigated layouts.

As already evidenced in Section 3.3, the adoption of the ellipsoidal shape reduces the thermal efficiency of the component due to increased surface-to-volume ratio. For the vessel analysed in this section, meeting the prescribed BOR requirement induces an insulation weight increase of 2.5% and a total tank mass increase of 2.2% when compared to the corresponding configuration with hemi-spherical domes. The associated optimized mass distribution across the tank layers and stored fuel is shown in Fig. 7*l*.

The influence of alternative composite lay-up is assessed leveraging the more pragmatic, thus, higher-fidelity tank model introduced in this section. Besides the quasi-isotropic sequence employed in previous analyses, additional lay-ups are tested, each consisting of the same number of plies to ensure consistency. These include balanced angle-ply configurations —such as the *magic angle* lay-up, specifically designed to optimally balance hoop and longitudinal loads in cylindrical structures [72]- as well as progressive and tailored symmetric laminates. Furthermore, the sequences $[11°/90°_2/\pm 25°/18°/90°/21°]$ and $[-87°/36°/47°/33°/-57°/-36°/-50°/-44°]$, derived from Ref. [73] and Ref. [74], respectively, are also examined. These lay-ups originate from the application of optimization algorithms specifically developed to enhance the performance of composite pressure vessels operating under high pressure differentials. The corresponding results, summarized in Table 6, are expressed in terms of relative mass penalties for both the composite layer and the whole tank. Among the configurations considered, the quasi-isotropic $[0°/90°/45°/-45°]_S$ sequence indeed yields the lowest total mass. In contrast, alternative lay-ups either result in increased structural weight or violation of mechanical constraints thereby being classified as unfeasible for the considered application. To make the optimizer converge to a feasible set of design variable, in fact, the technological thickness bounds reported in Table 4 must be relaxed.

Table 6
Assessment of alternative composite stacking sequences evaluated for the optimization of Tank VI. Feasibility is indicated along with the relative increase in CFRP outer layer mass (Δm_{CFRP}) and overall tank mass (Δm_{tank}) with respect to the baseline quasi-isotropic configuration.

Stacking sequence	Feasibility	Δm_{CFRP}	Δm_{tank}
$[0°/90°/45°/-45°]_S$	Yes	/	/
$[11°/90°_2/\pm 25°/18°/90°/21°]$	Yes	+5.1%	+0.8%
$[\pm 54.7°]_8$	Yes	+23.0%	+2.9%
$[\pm 45°]_8$	Yes	+23.6%	+3.0%
$[-87°/36°/47°/33°/-57°/-36°/-50°/-44°]$	Yes	+44.1%	+5.5%
$[90°/45°/30°/0°]_S$	Yes	+61.5%	+7.6%
$[\pm 30°]_8$	No	–	–
$[0°/15°/30°/45°]_S$	No	–	–

3.7. Comparative assessment of optimized tank architectures

This section provides an overview of each of the optimized vessel defined and analysed in the study, comparing their respective configurations and assessing the general influence design choices have on the storage system performance, summarized in Table 7.

The total mass – broken down by constituent layers – of each LH_2 tank configuration is reported in Fig. 8, where the significant performance advantage of composite-based architectures over fully metallic designs is evident. Significantly, the titanium outer layer of Tank *I* alone yields a 34% greater mass than the entire assembly of the corresponding Tank *II*, featuring the CFRP shell. Notably, even when accounting for the inclusion of all realistic features examined – as done in Tank *VI* –, the metallic layer still incurs in a 3.3×10^3 kg penalty over composite construction, resulting in a 57% difference in m_{tank} between the simple all-metal and foam Tank *I* and the most feature-packed vessel of configuration *VI*. Moreover, while the foam insulation mass, being mainly linked to thermal constraints, remains relatively unaffected by the adoption of either a metallic or composite shell, the inner liner of Tank *I*, somewhat concurrent to the tank load bearing capability, has almost twice the weight of the mean m_{Al} for vessels equipped with composite material.

The inclusion of essential features for operational viability has a clear detrimental effect on η_{tank}. Among these additions, the most influential is indeed the use of endcaps deviating from the hemi-spherical geometry. In the assumption of fixed internal volume, the integration of hemi-ellipsoidal domes necessitates thicker insulation to meet thermal constraints. The weight penalty is amplified by m_{CFRP} and, in particular, by the relative positioning of the structural and insulation layers. Since the structural layer is located externally to the foam – conforming to the outer PUR surface – any increase in t_{PUR} directly results in a larger and therefore heavier external shell. Similarly, the cutouts introduce both localized geometric discontinuities acting as stress concentrators requiring reinforcement to comply with structural constraints and thermal bridges, facilitating localized heat ingress and altering the vessel thermal performance. The integration of anti-sloshing bulkheads is responsible of a notable increase in the inner layer mass, however, since this layer accounts for a small percentage of m_{tank}, the global weight increase is rather contained. Nonetheless, even when accounting for these penalizing yet necessary additions the gravimetric efficiency of the designed vessels reaches appealing values, in the order of 50%, just 5% off the fundamental threshold identified in Ref. [8]. Finally, the proposed framework is intrinsically scalable to tanks of different capacities, owing to the dimension-independent thermo-mechanical governing equations and the enforced mesh density referenced in Section 2.4.1. In general, for smaller tank volumes, the larger surface-to-volume ratio enhances thermal losses, leading to higher fuel venting rates, which, for a certain BOR design requirement translates into reduced gravimetric efficiency. Conversely, thermal penalties are mitigated for larger vessels, resulting in improved overall efficiency, despite more challenging aircraft integration.

Table 7
Performance metrics of the optimized tank configurations.

		I	II	III	IV	V	VI
Performance	BOR	2.50% daily					
	η_{tank}	29.31%	50.11%	49.34%	50.00%	49.76%	49.22%

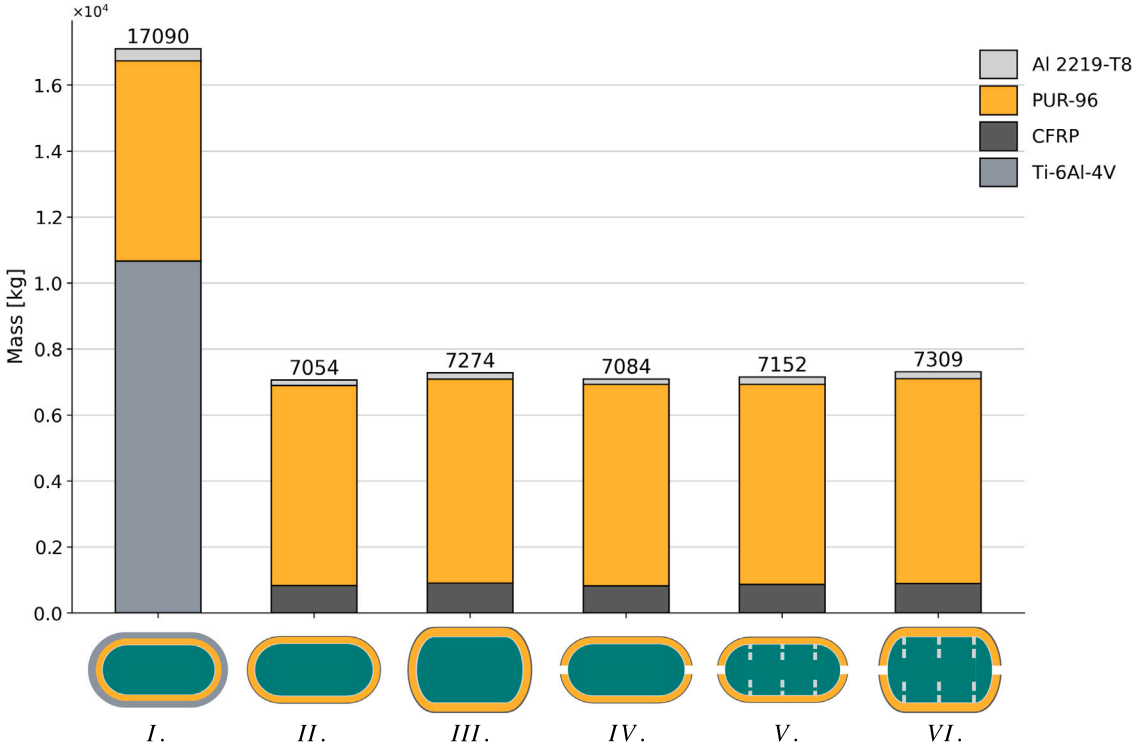

Fig. 8. Comparison of minimum achievable mass for each tank configuration, with breakdown by layer. The all-metal design (*I*) results in substantially higher total mass compared to composite architectures (*II* to *VI*). The improved mass efficiency enables the integration of realistic design features while pushing $\eta_{tank} \approx 50\%$.

3.8. Case study: integration of optimized LH_2 storage into a next-generation sustainable aircraft

The pressure vessel of configuration *VI.* is tailored for integration into a state-of-the-art LH_2-powered aircraft concept: the ultra-high aspect ratio strut-braced wing (UHARW) introduced by Wahler et al. [29], which targets performance characteristics comparable to those of popular airliners like the Airbus A320.

To meet the target design range of 3400 M, the total required liquid hydrogen mass is estimated at 6534 kg. Storage is distributed across two cryogenic tanks installed within the forward and aft fuselage sections, as illustrated in Fig. 9*a*). The rear tank is designed to conform to the full internal fuselage diameter (D_f), thereby maximizing volumetric efficiency. However, to comply with Certification Specification §25.772 – which mandates access between the flight deck and passenger cabin [75] – a reduced external diameter ($D_{t_{ext}}$) is enforced for the forward tank, ensuring the presence of a continuous access path. In this instance, a catwalk width of $W_{cw} = 58$ cm is adopted, being consistent with standard aisle dimensions for certified commercial aircraft [76], Fig. 9*b*). Furthermore, to maintain the aircraft's longitudinal centre-of-gravity within its design envelope, 60% of the cryogenic fuel is kept in the aft-tank and the remaining 40% is allocated to the forward unit. Hence, the two vessels are optimized, finding that, for the forward tank, the required foam thickness is ≈ 0.33 m, determining an inner cavity diameter ($D_{t_{int}}$) equal to 70% of D_f.

The thermo-mechanical behaviour of the optimized LH_2 storage units is assessed through the analysis of the representative field distributions shown for each layer in Fig. 10. For conciseness, only the plots corresponding to the highest magnitude fields are reported, without distinction between the forward and aft tanks due to the similarity of the resulting contour distributions. Equivalent stress contour plot in the inner metallic liner, including the integrated anti-sloshing baffles, is shown in Fig. 10*a*). Here, normalized peak stress reaches 61% of the allowable limit ($\bar{\sigma}_{SF}^{Al}$), suggesting that, if technologically possible, a moderate reduction in Al2219-T8 thickness could yield further mass savings without necessarily compromising structural integrity. The tank layer that appears to limit global resistance is the low-density insulating PUR. Specifically, as Fig. 10*b*) highlights, the safety-factor-adjusted yielding threshold is reached along the central restrained edge on the outer foam surface, hinting that

higher performance could be achieved either by employing advanced insulation materials that better balance low density and enhanced stiffness, or by re-evaluating the mechanical boundary conditions. In particular, less restrictive supports that allow for controlled dimensional variations or more evenly distributed reaction loads over a broader contact area may alleviate stress concentration, enhancing the structural behaviour. In fact, the regions of localized stress on the foam surface mainly arise from the combined effect of the presence of the anti-sloshing baffles and the tank-airframe mounting constraints, which locally restrict the natural thermal contraction of the layer. Hence, as the relatively low internal and hydrostatic pressures play a minor role on the tank mechanical response, the stress field is predominantly governed by thermally induced deformations. While less restrictive mechanical boundary conditions would indeed lower the stress magnitude [48], practical integration strategies and safety related considerations generally require a certain degree of over-constraining,

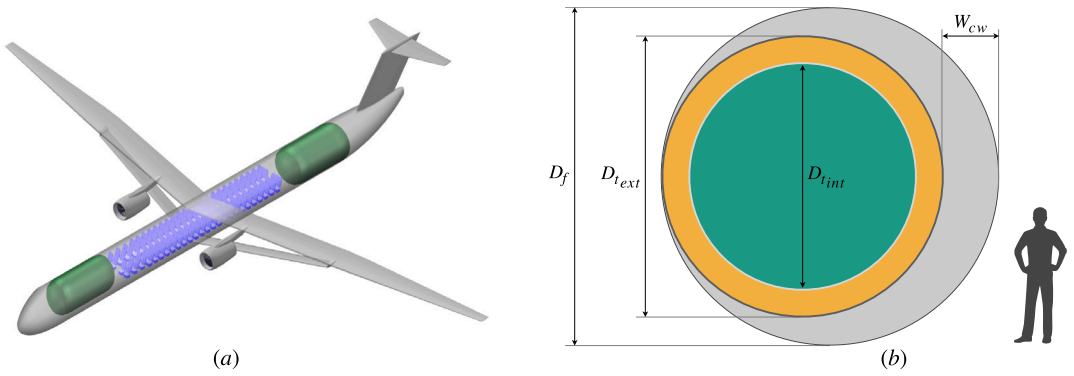

Fig. 9. (*a*) isometric view of the LH_2 strut-braced wing from Ref. [29]; (*b*) sectional view of the forward fuselage highlighting the vessel integration into the available volume, along with the standard-height civilian male for reference according to Ref. [76].

thereby rendering the assembly hyperstatic. Heat flux per unit area distribution in the insulating layer is reported in Fig. 10*c*), where the effects of the thermal penalty deriving from the cutout presence induces a localized increase in HFL. Finally, the structural performance of the outer composite shell is assessed through the Hashin damage initiation criterion, active in the fibre tension and matrix compression modes. Owing to the symmetric stacking sequence, the inner four plies yield analogous but lower-magnitude indices and are therefore omitted for conciseness. Thus the outer-most CFRP plies are discussed. Specifically, Fig. 10*d*) presents the contour plots of the Hashin fibre tension index, which attains its maximum value around the cutout-induced geometric discontinuity. Similarly, as shown in Fig. 10*e*, the maximum matrix compression index appears to be influenced by the airframe-component integration strategy, with the peak occurring near the three restrained circular edges. In both cases, the maximum values of HSNFTCRT and HSNMCCRT are consistently reached within the 90°-oriented ply. The low Hashin indices observed for the composite layer arise from the constraints imposed on the laminate architecture and from the coupled response of the multilayer vessel. The optimizer is restricted by the minimum allowable ply thickness, and the total number of plies is kept fixed to preserve laminate consistency across configurations; within these bounds, further reductions of the composite shell are not attainable. Moreover, the global structural behaviour is governed by the interaction among the constituent layers, with the PUR insulation acting as the limiting component from a stress perspective. Reducing the composite thickness would increase load transfer to the foam, causing its safety-factor-adjusted strength threshold to be exceeded. The resulting composite thickness therefore corresponds to the minimum value compatible with both the laminate constraints and the thermo-mechanical requirements of the multilayer system.

Having discussed the layer-wise thermo-mechanical response, as the global tank performance is considered, an additional observation emerges related to the influence of fuel capacity. The forward and aft-tanks, designed to contain 37% and 55% of reference V_{tank} respectively, are, in fact, indicative of scaling effects typical of cryogenic systems. In particular, reduced tank dimensions induce larger surface-to-volume ratios, increasing thermal ingress and specific insulation requirement [8]. Accordingly, the optimized gravimetric efficiency decreases from 49.22% for the reference Tank *VI*, on which the UHARW storage system is based, to 48.60% and 48.41% for the aft and forward tanks respectively, while maintaining the 2.50% daily BOR constraint active.

4. Discussion and future developments

The conceptual design of the passively-insulated sandwich-composite cryogenic pressure vessel is presented, outlining its advantages in performance, simplicity, and reliability over more complex actively cooled systems. Accordingly, a dedicated finite-element-based optimization framework, tailored to the layered tank layout, is developed. The tool enables a systematic exploration of the optimal vessel design space, targeting mass minimization while fulfilling thermal and mechanical constraints, with the general aim of achieving performance metrics that support hydrogen as a viable alternative to conventional aviation fuels and identifying areas of further improvement.

The assessment of several tank layouts reveals that while the use of the Al2219-T8 alloy is fitting for construction of the fuel containment liner, providing corrosion resistance and specific strength at cryogenic temperatures, a structurally superior metal is required for the manufacturing of the outer shell, thus, imposing penalties in terms of costs, manufacturability, and availability. An high-strength metallic compound, such as the Ti-6Al-4V alloy, represents a suitable candidate for the construction of the structural shell even though it induces significant mass penalty over composite use. Specifically, given the considered high-level pressure vessel requirements, maximum gravimetric efficiency for the optimized component is below 30%, with the metallic outer shell, on its own, representing more than 44% of the whole tank mass. Conversely, the use of carbon-fibre-reinforced composite material proves necessary to reach competitive storage system performance: compared to the metallic design, composite-based configurations reduce overall tank mass by up to 59%, improving η_{tank} by 21.8%.

From a geometric standpoint – apart from spherical vessels that would introduce volumetric penalties in vehicle integration – tanks with cylindrical section and hemi-spherical endcaps yield the most favourable thermo-mechanical response. Nonetheless, practical integration constraints may favour alternative dome geometries, like hemi-ellipsoidal endcaps, which – despite preserving the same internal volume as the hemi-spherical configuration – induce a 3.1% weight gain. This penalty arises from the less favourable surface-to-volume ratio, which increases heat ingress, thereby requiring greater insulation thickness to satisfy the prescribed boil-off rate limit, ultimately rising the overall tank mass. Furthermore, pragmatic features required for aircraft integration typically introduce stress concentrations and mass penalties, underlining the importance of accounting for their impact on tank performance from the conceptual design stage. For example, the inclusion of cutouts – combined with localized thermal loads to reflect the reduced insulation effectiveness in these regions – results in a marginal yet non-negligible increase in the required insulation thickness to maintain thermal performance targets. To mitigate uncontrolled fuel movement in vehicle applications the inclusion of anti-sloshing baffles is necessary even though their presence significantly increases the weight of the inner liner, by approximately 40% for the considered design. Nonetheless, given that this layer constitutes only 1.6% of total tank mass, the resulting impact on overall gravimetric efficiency is rather contained, being around 1%. Among the configurations analysed, the quasi-isotropic stacking sequence yields the minimum tank

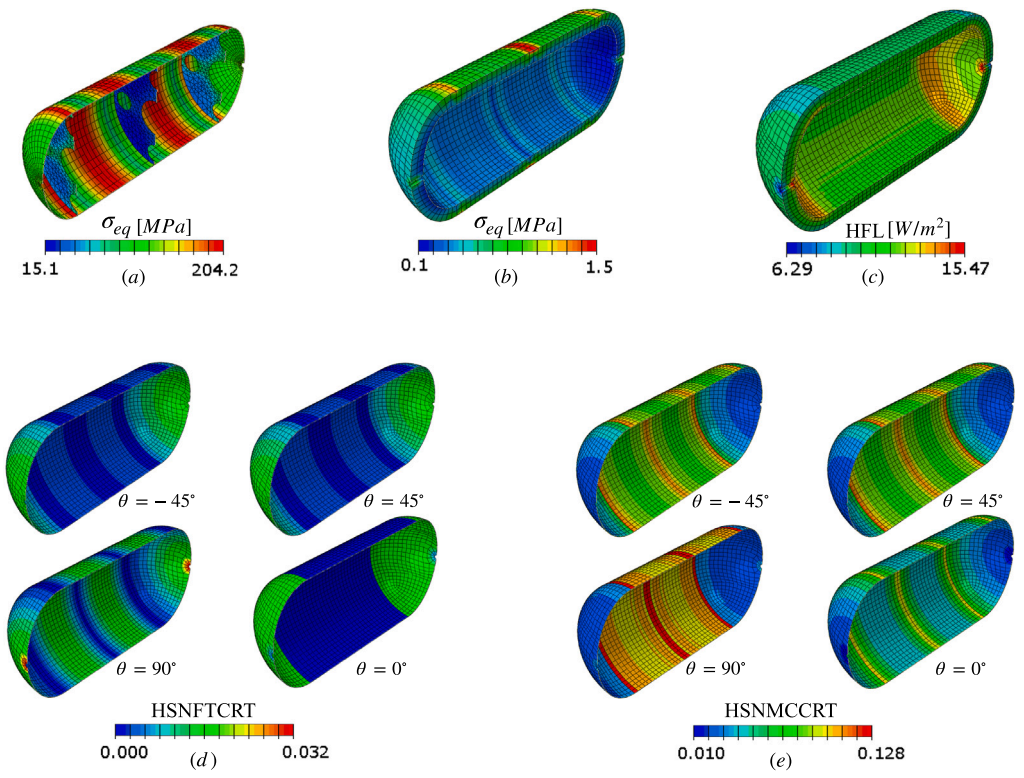

Fig. 10. Optimized UHARW vessels thermo-mechanical fields. Equivalent stress in the inner (*a*) and middle (*b*) layers; heat flux per unit area in the middle layer (*c*); Hashin fibre tension (*d*) and matrix compression (*e*) indices distribution for the four more loaded plies of the composite outer shell.

mass and should therefore be considered as a primary candidate for the manufacturing of composite vessels.

Ultimately, although the optimized composite-based designs presented in this study do not reach the $\eta_{\text{tank}} > 55\%$ threshold identified as critical for surpassing kerosene-fuelled aircraft in range and performance [25], through the use of the optimization framework developed, they do consistently achieve gravimetric efficiencies around 50%, even when accounting for practical integration features. Moreover, the analysis performed reveals that tailored component-airframe integration approaches and advanced insulating materials that conjugates low thermal conductivity, low diffusivity and high specific strength may be decisive in further improving the performance of the cryogenic layered architecture.

It is worth pointing out that multiple sources of uncertainty limit the accuracy of complex, multi-physics simulations. Such limitation arises not only from the variability of material properties under challenging cryogenic conditions, but also from boundary-conditions simplification, modelling assumptions, and idealized operating scenarios. Small deviations in thermal or mechanical parameters, for example deriving from manufacturing imperfections or fibre misalignment [77], or in operational conditions like different external heat-transfer coefficients, may locally affect stress and heat-flux distributions, though without significantly altering the overall design trends observed and described in this work. The formulation adopted in this study indeed treats these parameters as fixed inputs and therefore does not explicitly propagate their variability through the optimization process. Extending the framework to a reliability-based formulation – supported by experimental data for model calibration – would allow the systematic quantification of such effects, providing confidence intervals on design variables and a more rigorous assessment of the robustness of the optimal configuration.

Finally, it is acknowledged that the present framework does not include an explicit assessment of global or local buckling, despite its relevance for thin-walled pressure vessels. The adopted stress-based constraints offer only partial protection against instability, and future extensions of the framework should incorporate dedicated stability checks to ensure structural robustness.

Future work will focus on covering the gap in performance that may enable the environmentally and commercially sustainable adoption of LH_2 aviation tanks. Specifically, the methodology will be extended to allow for regional thickness variation within layers, based on spatial distributions of output variables. Moreover, future work will address the spatial integration challenge by exploring and optimizing tank geometries that depart from conventional cylinder-based vessels. This includes the development of conformal tanks specifically sized to fit within the aircraft wing, wingbox, and tail-cone sections, as well as integral vessels that combine the structural functions of both the storage system and the airframe.

5. Concluding remarks

This work presented a computational framework for the optimization of passively insulated, sandwich-composite LH_2 pressure vessels tailored for aviation applications and employed it to analyse a range of tank configurations, ultimately identifying a pragmatic architecture suitable for sustainable aircraft integration. By coupling multiphysics finite element modelling with nonlinear constrained optimization, the framework enables a systematic exploration of tank architectures under realistic operational and integration constraints, providing insight into the trade-offs that govern their performance. The study demonstrates that composite-based architectures consistently achieve superior performance over metallic counterparts, delivering substantial mass reductions and higher gravimetric efficiency, even when realistic design features such as cutouts, baffles, and non-spherical domes are included. It also underscores the influence of geometric scaling and integration strategy on tank performance. These results demonstrate the value of targeted optimization in enabling high-performance hydrogen storage systems and contribute to the development of scalable, certifiable solutions for future H_2-powered aircraft.

CRediT authorship contribution statement

Sergio Bagarello: Writing – original draft, Visualization, Validation, Software, Methodology, Investigation, Data curation, Conceptualization. **Ali Elham:** Writing – review & editing, Supervision, Methodology, Formal analysis, Conceptualization. **Ivano Benedetti:** Writing – review & editing, Supervision, Methodology, Funding acquisition, Formal analysis, Conceptualization.

Declaration of competing interest

The authors declare the following financial interests/personal relationships which may be considered as potential competing interests: Sergio Bagarello reports financial support was provided by European Union. If there are other authors, they declare that they have no known competing financial interests or personal relationships that could have appeared to influence the work reported in this paper.

Acknowledgements

S.B. and I.B. acknowledge the support by the European Union - NextGenerationEU - National Sustainable Mobility Center CN00000023, Italian Ministry of University and Research Decree n. 1033—17/06/2022, Spoke 12, CUP B73C22000760001.

References

[1] International Civil Aviation Organization. ICAO establishes global platform to secure financing for aviation sustainability projects. 2025, https://www2023.icao.int/Newsroom/Pages/ICAO-establishes-global-platform-to-secure-financing-for-aviation-sustainability-projects.aspx. [Accessed 18 February 2025].

[2] Hammad AW, Rey D, Bu-Qammaz A, Grzybowska H, Akbarnezhad A. Mathematical optimization in enhancing the sustainability of aircraft trajectory: A review. Int J Sustain Transp 2020;14(6):413–36.

[3] Ozturk F, Cobanoglu M, Ece RE. Recent advancements in thermoplastic composite materials in aerospace industry. J Thermoplast Compos Mater 2024;37(9):3084–116.

[4] Adler EJ, Martins JR. Blended wing body configuration for hydrogen-powered aviation. J Aircr 2024;61(3):887–901.

[5] Benad J, Vos R. Design of a flying v subsonic transport. In: 33rd congress of the international council of the aeronautical sciences. 2022.

[6] Ansell PJ. Review of sustainable energy carriers for aviation: Benefits, challenges, and future viability. Prog Aerosp Sci 2023;141:100919. http://dx.doi.org/10.1016/j.paerosci.2023.100919, Special Issue on Green Aviation.

[7] Wang B, Ting ZJ, Zhao M. Sustainable aviation fuels: Key opportunities and challenges in lowering carbon emissions for aviation industry. Carbon Capture Sci Technol 2024;13:100263. http://dx.doi.org/10.1016/j.ccst.2024.100263.

[8] Adler EJ, Martins JR. Hydrogen-powered aircraft: Fundamental concepts, key technologies, and environmental impacts. Prog Aerosp Sci 2023;141:100922. http://dx.doi.org/10.1016/j.paerosci.2023.100922, Special Issue on Green Aviation.

[9] Ren R, Wang Y, Li T. In situ growth of FeCo sulfides on cobalt iron foam for efficient high-current-density hydrogen evolution reaction electrocatalysis. J Colloid Interface Sci 2025;682:288–97. http://dx.doi.org/10.1016/j.jcis.2024.11.251.

[10] Yusaf T, Mahamude ASF, Kadirgama K, Ramasamy D, Farhana K, Dhahad HA, Talib ARA. Sustainable hydrogen energy in aviation - A narrative review. Int J Hydrog Energy 2024;52:1026–45. http://dx.doi.org/10.1016/j.ijhydene.2023.02.086.

[11] Hoelzen J, Silberhorn D, Zill T, Bensmann B, Hanke-Rauschenbach R. Hydrogen-powered aviation and its reliance on green hydrogen infrastructure–Review and research gaps. Int J Hydrog Energy 2022;47(5):3108–30.

[12] Brelje BJ, Martins JR. Electric, hybrid and turboelectric fixed-wing aircraft: A review of concepts, models, and design approaches. Prog Aerosp Sci 2019;104:1–19.

[13] Lán S, Špák M. Contrail formation assessment based on aerological data. Transp Res Procedia 2020;51:225–31. http://dx.doi.org/10.1016/j.trpro.2020.11.025, INAIR 2020 - CHALLENGES OF AVIATION DEVELOPMENT.

[14] Mukhopadhaya J, Rutherford D. Performance analysis of evolutionary hudrogen-powered aircraft. Int Counc Clean Transp 2022.

[15] Nicolay S, Karpuk S, Liu Y, Elham A. Conceptual design and optimization of a general aviation aircraft with fuel cells and hydrogen. Int J Hydrog Energy 2021;46(64):32676–94. http://dx.doi.org/10.1016/j.ijhydene.2021.07.127.

[16] Verstraete D, Hendrick P, Pilidis P, Ramsden K. Hydrogen fuel tanks for subsonic transport aircraft. Int J Hydrog Energy 2010;35(20):11085–98. http://dx.doi.org/10.1016/j.ijhydene.2010.06.060, Hyceltec 2009 Conference.

[17] Brewer G, Morris R. Study of LH2 fueled subsonic passenger transport aircraft. 1976, Contractor report NASA/CR—144935. NASA.

[18] Huete J, Pilidis P. Parametric study on tank integration for hydrogen civil aviation propulsion. Int J Hydrog Energy 2021;46(74):37049–62. http://dx.doi.org/10.1016/j.ijhydene.2021.08.194.

[19] Millis MG, Tornabene RT, Jurns JM, Guynn MD, Tomsik TM, Overbeke TJV. Hydrogen fuel system design trades for high-altitude long-endurance remotely-operated aircraft. 2009, NASA/TM-2009-215521.

[20] Samner IE. Low-density foam for insulating liquid- hydrogen tanks. Technical note NASA/TN-D5114, Ohio: Lewis Research Center Cleveland; 1969.

[21] Adler E, Martins J. Liquid hydrogen tank boil-off model for design and optimization. J Thermophys Heat Transfer 2024. http://dx.doi.org/10.2514/1.T7005.

[22] Gomez A, Smith H. Liquid hydrogen fuel tanks for commercial aviation: Structural sizing and stress analysis. Aerosp Sci Technol 2019;95:105438. http://dx.doi.org/10.1016/j.ast.2019.105438.

[23] Tzoumakis G, Fotopoulos K, Lampeas G. Multi-physics digital model of an aluminum 2219 liquid hydrogen aircraft tank. Aerospace 2024;11(2). http://dx.doi.org/10.3390/aerospace11020161.

[24] Mazzoni, Accardo, Biga, Brusa, Delprete, Manrique-Escobar, Vercella. Hydrogen storage system design: Case studies for airborne application. In: 34th congress of the international council of the aeronautical sciences, 09-13/09/2024. ICAS; 2024.

[25] Brelje BJ, Martins JR. Aerostructural wing optimization for a hydrogen fuel cell aircraft. In: AIAA scitech 2021 forum. 2021, p. 1132.

[26] Licheva G, Liscouet-Hanke S. Cryogenic tank sizing model for the conceptual design of hydrogen-powered aircraft. In: 34th congress of the international council of the aeronautical sciences, 09-13/09/2024. ICAS; 2024.

[27] Olsson R, Cameron C, Moreau F, Marklund E, Merzkirch M, Pettersson J. Design, manufacture, and cryogenic testing of a linerless composite tank for liquid hydrogen. Appl Compos Mater 2024;16:1131–54. http://dx.doi.org/10.1007/s10443-024-10219-y.

[28] Mantzaroudis VK, Theotokoglou EE. Computational analysis of liquid hydrogen storage tanks for aircraft applications. Materials 2023;16(6). http://dx.doi.org/10.3390/ma16062245.

[29] Wahler NFM, Ma Y, Elham A. Conceptual design and aerostructural trade-offs in hydrogen- powered strut-braced wing aircraft: Insights into dry and wet ultra-high aspect ratio wings. Aerospace 2025;12(2). http://dx.doi.org/10.3390/aerospace12020077.

[30] Brewer GD. Hydrogen aircraft technology. Routledge; 1991.

[31] Ivdre A, Abolins A, Volkovs N, Vevere L, Paze A, Makars R, Godina D, Rizikovs J. Rigid polyurethane foams as thermal insulation material from novel suberinic acid-based polyols. Polymers 2023;15(14). http://dx.doi.org/10.3390/polym15143124.

[32] Bagarello S, Campagna D, Benedetti I. A survey on hydrogen tanks for sustainable aviation. Green Energy Intell Transp 2024;100224. http://dx.doi.org/10.1016/j.geits.2024.100224, URL https://www.sciencedirect.com/science/article/pii/S2773153724000768.

[33] Dannet G. Integration of cryogenic tanks and fuel cells for future hydrogen-powered aircraft [Ph.D. thesis], Linkoping university, Department of Management and Engineering; 2021.

[34] Holt JMT, Ho CY, editors. Structural alloys handbook. In: 1996 edition. CINDAS/Purdue University; 1996.

[35] Simon N, Drexler E, Reed R. Review of cryogenic mechanical and thermal properties of Al-Li alloys and alloy 2219. 1990, p. 196.

[36] Lee JA, Woods S. Hydrogen embrittlement. Natl Aeronaut Space Adm Sci Tech Inf (STI) Program Off 2016.

[37] Li KC, Wu ZJ, Liu MJ, Xu XS, Xu W. An application of reinforced polyurethane foam in design of the common bulkhead for cryogenic tanks. In: Materials science forum, vol. 975, Trans Tech Publ; 2020, p. 182–7.

[38] Fesmire lE, Coffman B, Menghelli B, Heckle K. Spray-on foam insulations for launch vehicle cryogenic tanks. NASA technical paper NASA/TP 2011 20110014400, 2011, NASA Space Cryogenics Workshop, Idaho, July 2011, https://ntrs.nasa.gov/citations/20110014400.

[39] Sparks LL, Arvidson J. Thermal and mechanical properties of polyurethane foams and a survey of insulating concretes at cryogenic temperatures. National Bureau of Standards Boulder, CO.; 1984.

[40] Songhan Plastic Technology Co, Ltd. Overview of materials for Thermoset Polyurethane Foam, Unreinforced, Available on line https://www.lookpolymers.com/pdf/Overview-of-materials-for-Thermoset-Polyurethane-Foam-Unreinforced.pdf.

[41] Bartolomeu F, Gasik M, Silva FS, Miranda G. Mechanical properties of Ti-6Al-4V fabricated by laser powder bed fusion: A review focused on the processing and microstructural parameters influence on the final properties. Metals 2022;12(6). http://dx.doi.org/10.3390/met12060986.

[42] Vandenbroucke B, Kruth J. Selective laser melting of biocompatible metals for rapid manufacturing of medical parts. Rapid Prototyp J 2007;13(4). http://dx.doi.org/10.1108/13552540710776142.

[43] Wysocki B, Maj P, Sitek R, Buhagiar J, Kurzydłowski KJ, Święszkowski W. Laser and electron beam additive manufacturing methods of fabricating titanium bone implants. Appl Sci 2017;7(7). http://dx.doi.org/10.3390/app7070657.
[44] Horiuchi T, Ooi T. Cryogenic properties of composite materials. Cryogenics 1995;35(11):677–9.
[45] Gates TS, Su X, Abdi F, Odegard GM, Herring HM. Facesheet delamination of composite sandwich materials at cryogenic temperatures. Compos Sci Technol 2006;66(14):2423–35.
[46] Islam MS, Benninger LF, Pearce G, Wang C-H. Toughening carbon fibre composites at cryogenic temperatures using low-thermal expansion nanoparticles. Compos Part A: Appl Sci Manuf 2021;150:106613.
[47] Xue J, Wang W, Zhang J-Z, Wu S-J. Progressive failure analysis of the fiber metal laminates based on chopped carbon fiber strands. J Reinf Plast Compos 2015;34:364–76. http://dx.doi.org/10.1177/0731684415571659.
[48] Bagarello S, Campagna D, Benedetti I. Computational thermo-mechanical modelling and design-space exploration of cryogenic hydrogen tanks for aviation. Aerosp Sci Technol 2026;168:110755. http://dx.doi.org/10.1016/j.ast.2025.110755, URL https://www.sciencedirect.com/science/article/pii/S1270963825008260.
[49] Mital S, Gyekenyesi J, Arnold S, Sullivan R, Manderscheid J, Murthy P. Review of current state of the art and key design issues with potential solutions for liquid hydrogen cryogenic storage tank structures for aircraft applications. 2006, NASA - Technical Memorandum (TM).
[50] National Research Council Committee on Air Quality in Passenger Cabins of Commercial Aircraft. The airliner cabin environment and the health of passengers and crew. 2002, Washington(DC) PMID: 25032286.
[51] Curto D, Franzitta V, Guercio A, Martorana P. FEM analysis: A review of the most common thermal bridges and their mitigation. Energies 2022;15(7). http://dx.doi.org/10.3390/en15072318, URL https://www.mdpi.com/1996-1073/15/7/2318.
[52] H2FLY. H2FLY accelerates progress towards zero-emission commercial flight. 2023, https://www.h2fly.de/2023/04/05/h2fly-accelerates-progress-towards-zero-emission-commercial-flight-3/. [Accessed 9 March 2025].
[53] Smith M. ABAQUS/Standard user's manual, version 6.9. United States: Dassault Systèmes Simulia Corp; 2009.
[54] Flanagan DP, Belytschko T. A uniform strain hexahedron and quadrilateral with orthogonal hourglass control. Internat J Numer Methods Engrg 1981;17(5):679–706.
[55] Belytschko T, Ong JS-J, Liu WK, Kennedy JM. Hourglass control in linear and nonlinear problems. Comput Methods Appl Mech Engrg 1984;43(3):251–76.
[56] Federal Aviation Administration. §25.303 Factor of Safety. 2023, URL https://www.ecfr.gov/current/title-14/part-25, Title 14 Code of Federal Regulations (CFR), Part 25, U.S. Government Publishing Office.
[57] The MathWorks Inc. MATLAB version: 9.13.0 (R2022b). 2022, URL https://www.mathworks.com.
[58] Poon N, Martins J. An adaptive approach to constraint aggregation using adjoint sensitivity analysis. Struct Multidiscip Optim 2007;34:61–73. http://dx.doi.org/10.1007/s00158-006-0061-7.
[59] AircraftMaterialsUKLtd Reg Co. Aluminium alloy 2219 - Technical data sheet. 2025, https://www.aircraftmaterials.com/data/aluminium/2219.html. [Accessed 05 May 2025].
[60] Mo C, Xu Y, Yuan S. Analysis of thickness variation in 2219 aluminum alloy ellipsoid shell with differential thickness by hydroforming. Metals 2024;14(10). http://dx.doi.org/10.3390/met14101140, URL https://www.mdpi.com/2075-4701/14/10/1140.
[61] Nguyen HD, Pramanik A, Basak A, Dong Y, Prakash C, Debnath S, Shankar S, Jawahir I, Dixit S, Buddhi D. A critical review on additive manufacturing of Ti-6Al-4V alloy: Microstructure and mechanical properties. J Mater Res Technol 2022;18:4641–61.
[62] Materialise NV. Titanium for 3D printing. 2024, URL https://www.materialise.com/en/industrial/3d-printing-materials/titanium. [Accessed 14 June 2025].
[63] Malekinejad H, Ramezani F, Carbas RJC, Marques EAS, da Silva LFM. Study of CFRP laminate gradually modified throughout the thickness using thin ply under transvers tensile loading. Materials 2024;17(10). http://dx.doi.org/10.3390/ma17102388, URL https://www.mdpi.com/1996-1944/17/10/2388.
[64] Wang B, Wen L, Xiao J, Wang S, Ren P, Wang L, Zu L, Hou X. Automated fiber placement path planning and analysis of pressure vessels. Materials 2023;16(18). http://dx.doi.org/10.3390/ma16186187, URL https://www.mdpi.com/1996-1944/16/18/6187.
[65] Triton Alloys Inc. Aluminum 2219 plate supplier exporter stockist dealer. 2024, https://www.tritonalloysinc.com/2219-aluminum-plate.html. [Accessed 17 July 2025].
[66] AM-Material. Introduction to Ti-6Al-4V titanium alloy. 2023, https://am-material.com/news/introduction-to-ti-6al-4v-titanium-alloy/. [Accessed 17 July 2025].
[67] Airbus. How to store liquid hydrogen for zero-emission flight. 2021, https://www.airbus.com/en/newsroom/news/2021-12-how-to-store-liquid-hydrogen-for-zero-emission-flight. [Accessed 09 July 2025].
[68] ZeroAvia. ZeroAvia awarded UK government grant for development and flight test of liquid hydrogen fuel system. 2023, https://zeroavia.com/zeroavia-awarded-uk-government-grant-for-development-and-flight-test-of-liquid-hydrogen-fuel-system/. [Accessed 09 July 2025].
[69] Krishna R. Hydrogen storage for energy application. 2012.
[70] Demaco Cryogenics. Vacuum insulated transfer lines for LH_2. 2024, URL urly.it/318t72. [Accessed 11 March 2025].
[71] Lei Y, Zhang L, Zhong S, Huang B. Multi-objective optimization of a T-shaped anti-sloshing baffle based on NSGA-II. Front Energy Res 2022;10. http://dx.doi.org/10.3389/fenrg.2022.810937.
[72] Demirkoparan H, Pence TJ. Magic angles for fiber reinforcement in rubber-elastic tubes subject to pressure and swelling. Int J Non-Linear Mech 2015;68:87–95. http://dx.doi.org/10.1016/j.ijnonlinmec.2014.05.008, Mechanics of Rubber - in Memory of Alan Gent. URL https://www.sciencedirect.com/science/article/pii/S0020746214001103.
[73] Liang J, Ning Z, Li Y, Gao H, Liu J, Tian W, Zhao X, Jia Z, Xue Y, Miao C. An efficient optimization method for stacking sequence of composite pressure vessels based on artificial neural network and genetic algorithm. Appl Compos Mater 2024;31:1–24. http://dx.doi.org/10.1007/s10443-024-10201-8.
[74] Almeida JHS, Ribeiro ML, Tita V, Amico SC. Stacking sequence optimization in composite tubes under internal pressure based on genetic algorithm accounting for progressive damage. Compos Struct 2017;178:20–6. http://dx.doi.org/10.1016/j.compstruct.2017.07.054, URL https://www.sciencedirect.com/science/article/pii/S0263822317320317.
[75] European Union Aviation Safety Agency - Easy Access Rules for Large Aeroplanes (CS-25). §25.772 Pilot compartment doors. 2023, https://www.easa.europa.eu/en/document-library/easy-access-rules/online-publications/easy-access-rules-large-aeroplanes-cs-25?page=26. [Accessed June 2025].
[76] Raymer DP. Aircraft design: A conceptual approach, In: AIAA education series, 4 ed. Reston, Va: American Institute of Aeronautics and Astronautics; 2006, URL http://www.loc.gov/catdir/toc/ecip068/2006004706.html.
[77] Warkina R, Regassa Y. Optimizing performance of hybrid fiber reinforced overwrapped pressure vessel. J Compos Mater 2025;59(2):187–206.